Impact of proton radiation on the performance of single-junction perovskite solar cells for space applications

Harini Srikanth Rao [a], Wei-Hao Chiu [b], Shih-Hsuan Chen [a], Ming-Chung Wu [a,b,c,d], Kun-Mu Lee [a,b,c,e,*]

[a] *Department of Chemical and Materials Engineering, Chang Gung University, Taoyuan, 33302, Taiwan*
[b] *Center for Sustainability and Energy Technologies, Chang Gung University, Taoyuan, 33302, Taiwan*
[c] *Division of Neonatology, Department of Pediatrics, Chang Gung Memorial Hospital, Linkou, Taoyuan, 33305, Taiwan*
[d] *Department of Materials Engineering, Ming Chi University of Technology, New Taipei, 243303, Taiwan*
[e] *College of Environment and Resources, Ming Chi University of Technology, New Taipei City, 4301, Taiwan*

ARTICLE INFO

ABSTRACT

The operational stability of the single-junction perovskite solar cells (PSCs) under space conditions remains a concern. This review systematically analyzes the effects of proton irradiation on PSCs, correlating the observed degradation with displacement damage and electronic ionization mechanisms. The penetration depth of protons and the associated vacancy profiles across PSC layers are assessed using Monte-Carlo simulations. Proton irradiation generates defects in the perovskite lattice, leading to reduced carrier mobility and device performance. Substrate analysis shows that cerium-doped glass, fused quartz, and silica retain optical clarity better than soda lime glass and flexible substrates. Transparent conductive oxides (TCOs) like Indium-tin oxide (ITO) exhibit strong radiation stability compared to other TCOs. For charge transport layers (CTLs), inorganic CTLs demonstrated better radiation resistance compared to their organic counterparts. The phenomenon of self-recovery in PSCs is also explored, which is attributed to defect recovery, relaxation of ion migration, and thermal annealing. By integrating experimental findings with simulation-based insights, this review maps the vulnerability of each device layer and addresses the proton irradiation relevant for space environments.

1. Introduction

Solar energy has emerged as an essential power source for terrestrial and space applications due to its renewable nature and ability to meet high energy demands. As numerous upcoming space missions, such as NASA's Dragonfly, ASTHROS, CLARREO, and DAVINCI, are being designed to operate in harsh extraterrestrial environments, the demand for reliable, efficient, and lightweight power systems has become critical [1–4]. Solar cells, being compact and self-sustaining, are strong candidates to fulfill these energy requirements. Since their first deployment in 1958 to power a satellite, they have remained the backbone of space missions [5,6]. Photovoltaic (PV) devices, containing semiconductor materials as an active layer, generate electron-hole pairs upon absorbing light [7–10]. The operation of PV devices involves three key processes: generating electron-hole pairs from photon absorption, separating these carriers in opposite directions using transport layers, and collecting the carriers in an external circuit to deliver power [11]. Due to the

abundance of silicon, most of the PV market is dominated by crystalline-silicon (c-Si) based PV devices. However, c-Si-based devices suffer from high production costs and limited theoretical and experimental power conversion efficiency (PCE) [7,12–16].

To overcome these limitations, researchers have explored alternative materials, such as III-V compound semiconductors, gallium arsenide (GaAs), copper indium gallium selenide (CIGS), cadmium telluride (CdTe), and perovskites [17,18]. Among these, perovskites have emerged as promising candidates due to their low production cost and high PCE. The PCE of perovskite solar cells (PSCs) has increased significantly from 3.8 % in 2009 to a certified value of 27 %, approaching the Shockley-Queisser efficiency limit (33.7 %) [19–22]. Unlike c-Si-based devices, PSCs can be manufactured at low temperatures [23]. Key advantages of perovskites include solution processability, tunable band gap, high specific power (power/weight ratio), and superior optoelectronic properties [24–28]. Notably, PSCs demonstrated a specific power of 23–29 W g^{-1} compared to 0.5 W g^{-1} for commercial

---

GaAs solar cells and 3W.g^{-1} for III-V semiconductor cells [24,29,30]. Moreover, their compatibility with lightweight, flexible substrates further enhances their potential for space applications [31].

If PSCs are employed in space missions, they must endure harsh space environments, including strong radiation, ultra-high vacuum, atomic oxygen, and severe temperature cycling [32,33]. The replacement of solar cells is not feasible once deployed in space, making the stability of solar cells against these harsh conditions an important factor to consider. Strong radiation includes gamma rays, neutrons, alpha particles, electrons, ultraviolet (UV) rays, beta particles, X-rays, and protons [34,35]. In this review, the effects of proton irradiation on PSCs are examined. In particular, when focusing on the effects of proton radiation, the evidence indicates that c-Si solar cells exposed to 150 keV protons experience a significant performance decline, with their open-circuit voltage (V_{oc}) dropping by over 40 % and their current density (J_{sc}) by about 10 % at a fluence of 10^{13} protons/cm^2 (p/cm^2) [29,36]. Protons introduce mid-gap defects in Si materials and decrease their diffusion length [37,38]. GaAs solar cells begin to show degradation at much lower fluence levels (around 10^{10} p/cm^2), while PSCs only start to degrade when exposed to fluences as high as 10^{15} p/cm^2 [29]. The comparison of before and after proton irradiation PCE for various types of solar cells is given in Fig. 1. While the data comes from different proton energies and fluences, the overall trend suggests that PSCs are less affected by proton exposure than most conventional technologies. As reported by, under identical conditions of 68 MeV protons at a fluence of 10^{13}p/cm^2, perovskite tandems retained ~94 % of their initial PCE, compared with <78 % for III-V (GaAs-based) 3J cells, providing a more direct benchmark across technologies. Direct side-by-side comparisons remain limited in the literature, and addressing this gap will be important for a fairer assessment of radiation harness across technologies [39]. It should be noted that Fig. 1 also includes tandem configurations (perovskite/CIGS and perovskite/SHJ) for completeness, but the focus of this review is on single-junction PSCs. Multi-junction devices are briefly acknowledged here due to their importance for space applications but are not discussed in detail, as a dedicated review would be more appropriate. Additionally, PSCs possess an interesting ability to recover from radiation damage, making them a potential option for space missions [31].

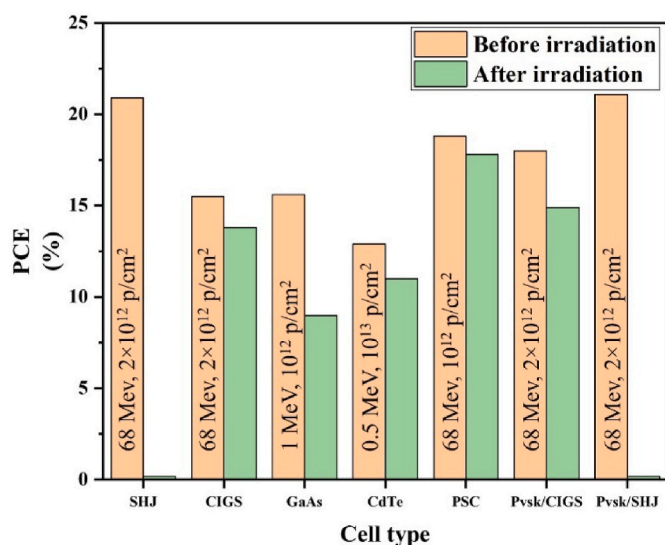Even though PSCs have better proton resilience than other solar cells,

Fig. 1. The comparison of PCE for different types of solar cells after proton irradiation [27,40–42]. Here, SHJ stands for silicon heterojunction and Pvsk for perovskite. The values written inside the bar 'before irradiation' are the energy and fluence of the proton beam. (For interpretation of the references to color in this figure legend, the reader is referred to the Web version of this article.)

it is still important to study the effects of proton irradiation on PSCs to further enhance their stability and performance in space conditions. The exact mechanism by which energy dissipates within a complex semiconducting perovskite environment is not yet fully understood [43]. In this review, a detailed discussion is provided on how protons interact with the PSCs, including displacement damage and ionization processes [44]. The Stopping and Range of Ions in Matter (SRIM) findings are summarized to support the experimental results, such as vacancy generation caused by protons, electronic energy loss, recoil energy loss, and penetration of the proton beams in the PSCs. SRIM is used to do the Monte-Carlo simulation that is based on the binary-collision approximation [27,45]. Furthermore, the interaction mechanisms within the PSC are strongly influenced by the energy of the incident protons. The effects of proton irradiation on the various layers of the PSCs, including substrates, electrodes, and charge transport layers (CTL), are explored. The radiation resistance of different substrates is discussed, along with the superior proton resilience of the inorganic CTLs over the organic ones. An important and unexpected property of PSCs to self-heal following proton irradiation is explored. Finally, changes in PV parameters across different device structures and proton energies are briefly addressed.

2. Space radiation

2.1. Space environment

The harsh conditions of space present significant challenges to both human missions and the materials used in spacecraft. Spacecraft must endure a variety of environmental stressors, such as extreme temperature variations, ranging from intense heating under direct sunlight to extreme cold in darkness, near-vacuum conditions that can reach as low as 7.5×10^{-15} torr in deep space, high UV flux, low-intensity low-temperature (LILT) conditions, and atomic oxygen (AtOx) in near-Earth space [33,46–49]. In addition, the solar spectrum in space is AM0, which is more intense and spectrally distinct from the AM1.5G spectrum typically used on Earth [50]. UV radiation in orbits such as low Earth orbit (LEO), medium Earth orbit (MEO), geosynchronous Earth orbit (GEO), and on the moon is significantly higher than on Earth, while LILT conditions are mainly encountered in the vicinity of Jupiter, Saturn, and deep space, where solar intensities drop to ~1.52 W/m^2 and temperatures can reach −170 °C [48,51]. AtOx exposure, particularly relevant to LEO and International Space Station (ISS), has fluxes of ~10^{12}-10^{15} atoms · cm^{-2} · s^{-1} with energies ~4.5–5eV, leading to surface erosion, corrosion of metal contacts, and oxide formation that accelerate PSC degradation [52–54].

Before deploying PSCs in space, it is crucial to evaluate how they will withstand these stressors. Several studies have been conducted on PSCs by replicating these environments. Table 1 displays these environmental properties across various space environments. These environments include Earth, LEO, MEO, GEO, the moon, and various planets. The solar intensity remains nearly the same as the solar constant across regions such as Earth, LEO, MEO, GEO, and the Moon [55]. As the distance from the Sun increases, the intensity of solar radiation decreases, leading to low-intensity conditions [56]. Table S1 (Supplementary Information) summarizes the effects of these stress factors on PSCs along with the corresponding mitigation strategies.

Beyond the broad environmental challenges, understanding the specific radiation conditions is crucial for designing durable spaceborne devices. Within Earth's magnetosphere, the Van Allen belts strongly influence the operational stability of solar cells and spacecraft electronics. Spacecraft operate within Earth's magnetosphere (Fig. 2(a)), a region that contains trapped radiation zones known as the Van Allen belts. These belts are divided into two primary regions: the inner belt (1000–6000 km), consisting mainly of high-energy protons from neutron decay [44,71–73] and the outer belt (13,000–60,000 km), dominated by electrons with energies up to 30 MeV [72].

Table 1

Environmental properties in various space environments, including Earth, LEO, MEO, and GEO, the Moon, Mars, Jupiter, and Saturn.

Space environment	Solar intensity (W/m^2)	UV intensity (W/m^2)	Temperature range ($^\circ$C)	Cycle duration	Vacuum level (torr)
Earth	~1370 [48]	0.1073 [57]	−20 °C–80 °C [58]	365.24 days [59]	760 [60]
LEO and MEO	~1370 [55]	139.6 [56]	−120 °C–120 °C [61]	1.5 h [56]	10^{-6} - 10^{-7} [62]
GEO	~1370 [55]	139.6 [56]	−196 °C–128 °C [63]	4.06 days [63]	10^{-12} [64]
Moon	~1370 [65]	139.6 [56]	−171 °C–112 °C [63]	28.1 days [63]	2×10^{-12} [65]
Mars	586.2 [66]	58.62 [56]	−143 °C–27 °C [63]	1.03 days [63]	4.77 [66]
Jupiter (Jovian atmosphere)	45.2 [48]	4.52 [56]	Average −145 °C [67]	Temperature depends on the pressure [68]	$>7.5 \times 10^5$ [68]
Saturn	15.2 [48]	1.52 [56]	−173 °C–57 °C [69]	Temperature depends on the pressure [70]	$>7.5 \times 10^5$ [70]
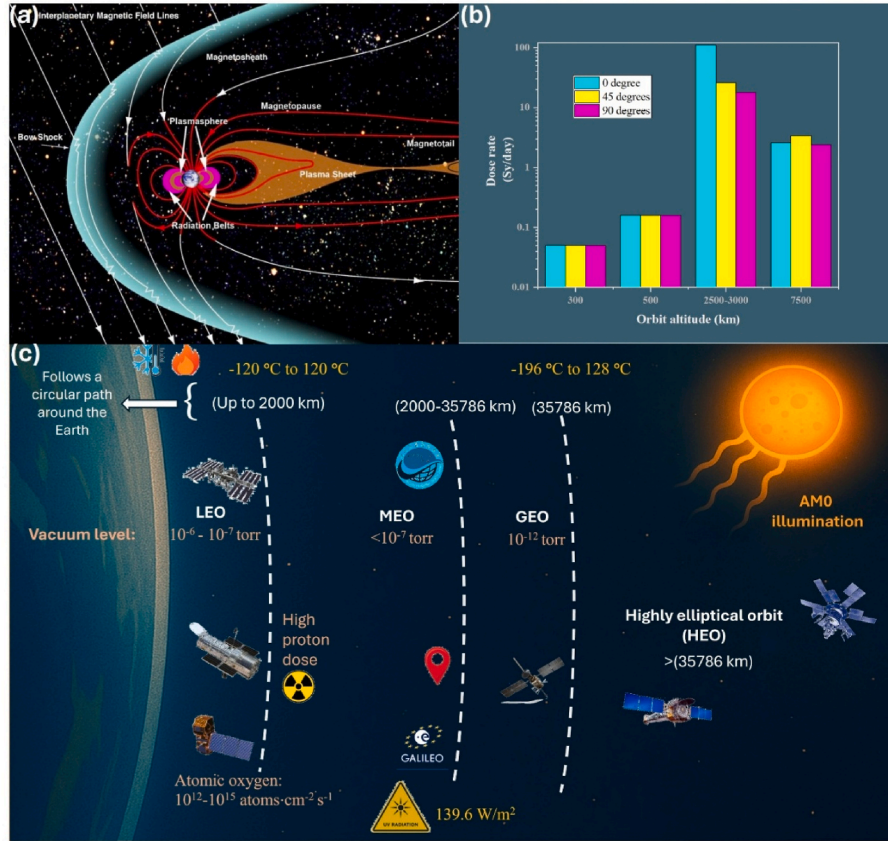
Fig. 2. (a) Illustration of Earth's Magnetosphere [71], (b) Dose rate (Sv/day) due to protons in the inner zone, depending on the inclination of the orbit and its altitude [44,76], (c) Illustration of Earth's Orbital Regions: LEO, MEO, GEO, and HEO.

The exposure of spacecraft to these belts depends strongly on their orbital altitudes [44]. Fig. 2(b) gives the dose rate of protons in the inner zone, and the corresponding data in Table S1. A detailed illustration of the Earth's orbitals is given in Fig. 2(c). LEO (e.g., ISS at ~400 km), lies below the inner belt and generally avoids direct radiation exposure, except when passing through the South Atlantic Anomaly. MEO intersects both belts, making it particularly harsh. As shown in Fig. 2(b) and (c), the dose rate peaks in the altitude range of approximately 2500 to 3000 km. This altitude falls within the MEO region, indicating that satellites operating in this zone are exposed to higher levels of radiation. In contrast, GEO (~35,786 km) lies just outside the outer belt but remains susceptible to space weather variations and high-energy particles originating from solar events. Certain spacecraft operate in Highly Elliptical Orbits (HEO), which traverse both belts, causing prolonged and repeated exposure [72,74,75]. Due to this uneven distribution of space radiation, satellites in different orbits require different levels of radiation hardness [44]. In addition to trapped belt particles, galactic cosmic rays (GCRs), composed predominantly of protons and alpha particles, also contribute to the overall space radiation environment.

These particles are capable of penetrating standard spacecraft shielding, such as aluminum with a thickness of 100 mils, and can cause damage to sensitive electronic components. At a distance of 1 astronomical unit from the Sun, the average proton density from GCRs has been measured to be approximately 8–9 protons/cm^3 [44].

Strong radiation is one of the primary stressors that PSCs would be subjected to in space. This includes a variety of particles and rays, such as gamma rays, alpha particles, electrons, protons, neutrons, and some ions, which travel through space with kinetic energies ranging from a few eVs to hundreds of GeVs. The origin of these particles is from the GCRs as well as some of the solar particles emitted by the Sun during solar eruptions [77,78]. Table 2 outlines the distinct characteristics of space radiation sources, showing that lower-energy environments like the solar wind have intense particle flux, while higher-energy sources such as GCRs and solar flares present greater radiation hazards despite their relatively lower flux.

Given the diversity of space radiation, it is important to briefly consider the characteristics and effects of different types of radiation, including gamma rays, neutrons, and charged particles, before focusing

Table 2

Energy and flux of particles from various sources [77–79].

Source	Particles	Energy (MeV)	Flux (cm^{-2}s^{-1})
Van Allen outer belt	e$^-$	0.001–30	10^3–10^7
Van Allen inner belt	p$^+$	0.001–100	10–10^6
Solar wind	p$^+$, e$^-$, α	<0.001	3×10^8
Solar flare	p$^+$, ions, gamma rays	1–10^3	10^{10}
GCRs	p$^+$, e$^-$, α, heavy ions	1–10^4	1–10

specifically on proton irradiation. Each type of radiation presents unique interaction mechanisms and damage profiles in PSCs, with various examples highlighting their significance. Gamma-ray tolerance of the PSCs is particularly important as the stability threshold of 100–1000 Gy is often used as a benchmark for space mission requirements [80]. For reference, the gamma dose rate on the Moon varies from 3.33 to 3.76 mSv/year [81]. The perovskite layer, composed of FA$_{0.945}$MA$_{0.025}$Cs$_{0.03}$Pb(I$_{0.975}$Br$_{0.025}$)$_3$, exhibited partial transition to the δ-phase of FAPbI$_3$ under gamma irradiation (Table S1), degrading crystallinity and introducing trap states that hinder carrier transport. However, the dominant contributor to performance loss was the radiation-induced coloring of the glass substrate, which significantly lowered optical transmittance and limited photon flux to the active layer. As a mitigation strategy, the authors proposed replacing the glass with flexible substrates like polyethylene naphthalate (PEN) and polyethylene terephthalate (PET), preventing the formation of color centers and reducing device weight. Additionally, applying radiation-hardened coatings or encapsulants could further suppress optical degradation in the substrate [82]. However, as discussed in a later section, flexible substrates did not exhibit good resistance under proton irradiation, indicating that further research is necessary to identify substrate materials that can withstand gamma and particle radiation in space environments.

Neutrons are a major concern in space following gamma radiation due to their deep penetration and strong nuclear interactions. Neutrons generated by spallation of GCRs with lunar regolith show fluxes spanning ~10^{-1} to 10^{13} neutrons cm^{-2} year^{-1} MeV^{-1} across energies from 10^{-9} to 10^4 MeV. The highest values of the flux are observed in the basalt-rich regions [81]. These elevated flux levels surpass terrestrial background and are relevant to environments like the ISS, where the fluence reaches ~2.8×10^{11} neutrons cm^{-2} year^{-1} for neutrons of energy ranging 0.1eV to 10^5 MeV [83]. Their pervasive presence and potential for damage make them critical to assess in space radiation studies. Rossi et al. examined the impact of fast neutron irradiation on flexible PSCs with spiro-OMeTAD and Benzothiadiazole–Poly(3-hexylthiophene) (BTD-P3HT) as hole transport layers (HTLs) under space-relevant fluences. While both devices degraded (Table S1), BTD-P3HT-based cells exhibited more stable charge transport and reduced recombination sensitivity under light variation [83]. This study highlights the critical influence of HTL-perovskite interfaces in determining neutron tolerance for space applications.

In contrast to gamma rays and neutrons, electrons are charged particles and exhibit different interaction mechanisms in space. Meredith et al. analyzed data from the INTEGRAL satellite and reported that in GEO, the decade-level peak flux of electrons ranges from 4.35×10^6 to 1.16×10^5 cm^{-2} s^{-1} sr^{-1} MeV^{-1} for energies between 0.69 MeV and 2.05 MeV. In MEO, the corresponding flux levels are significantly higher, ranging from 1.36×10^7 to 5.34×10^5 cm^{-2} s^{-1} sr^{-1} MeV^{-1}. These elevated fluxes contribute substantially to the radiation exposure experienced by satellites traversing or operating in these regions [84]. Song et al. conducted electron irradiation tests on high-efficiency PSCs using 1 MeV electrons. Their findings suggest that while high-energy electron irradiation primarily impacts light absorption and photocurrent generation, the core device architecture remains resilient (Table S1) [85].

Having addressed the effects of gamma radiation, neutrons, and

electrons, it is appropriate to now consider proton irradiation, a dominant component of the space radiation environment known for its significant impact on the structural and electronic stability of PV materials. Fig. 3 (Table S4) shows the dependence of the annual proton fluence on the proton energy in the different space environments as simulated by the SPace ENVironment Information (SPENVIS) [86,87]. It illustrates the exposure range that PSCs may experience in various environments. The graph shows that annual proton fluence decreases with increasing energy and generally increases with distance from Earth. A distinct dip at the equatorial orbit (~800 km) is due to strong geomagnetic shielding, while higher fluences appear in polar, upper LEO, GEO, and deep space regions [88]. Lower-energy protons contribute the highest fluence across all orbital locations. Among various stressors that PSCs will be subjected to in space, the proton is considered one of the critical factors that need special attention. The protons can fully penetrate the solar cell and break the covalent bonds in the perovskite layer, creating defect states and reducing PV performance, making it a critical factor [89,90]. As this review aims to explain the effects of proton irradiation on the stability and performance of PSCs, the following section discusses the irradiation conditions and testing protocols.

2.2. Irradiation protocols

In evaluating the irradiation protocols for PSCs, it is important to understand various standards that guide testing procedures, such as the AIAA (from the American Institute of Aeronautics and Astronautics), ECSS (from the European Cooperation for Space Standardization), and the testing done in NASA. The AIAA standard broad proton exposures spanning 20 keV to 3 MeV, using Equivalent Fluence and Displacement Damage Dose approaches to quantify energy-dependent degradation through relative damage coefficients or non-ionizing energy loss (NIEL) based models [91]. In contrast, the ECSS standard narrows the testing to two fixed energies, typically 1 MeV and 3 MeV, with strict flux control to ensure uniform and comparable degradation across different grades of solar cells [92]. Distinct from both, NASA's Marshall Space Flight Center focuses on lower proton energies (0.04–0.7 MeV) to study surface-related damage in solar cells and array components, particularly the deterioration of cover glasses and coatings that impact end-of-life
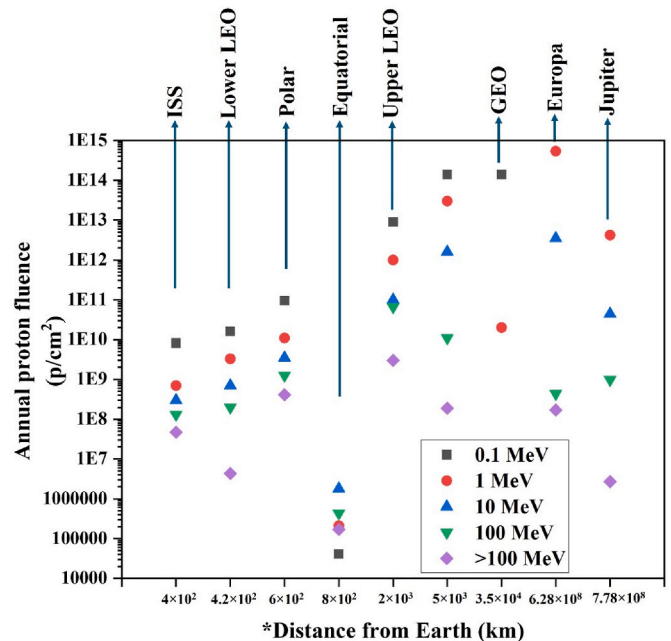

Fig. 3. Annual proton fluence in various space environments for energies: 0.1, 1, 10, 100, and >100 MeV (* x-axis is not drawn to scale) [32,40,86–88].

performance (EOL) [93]. Collectively, these protocols establish a coherent framework for qualifying solar cells under proton irradiation for space applications. Various energy/fluence protocols and accelerator facilities have also been used to simulate proton exposure; further details can be found in Table S2.

This section has outlined the harsh space environment that challenges PSCs. It has also described the different orbital regions, including LEO, MEO, GEO, and HEO, along with their distinct radiation profiles. Furthermore, the section has reviewed the standard testing methods used to simulate these environmental conditions, emphasizing proton irradiation due to its significant impact on device performance. This overview provides the foundation for the next section, which examines the specific effects of proton irradiation on PSCs and their constituent layers.

3. Proton radiation interaction mechanisms and their effects on PSCs

The subsequent section will explore the nuclear and electronic effects observed in PSCs after exposure to proton irradiation across a range of energies. This discussion will examine the impact on various structural layers of the PSCs, including the perovskite film, substrates, electrodes, and CTLs, which are crucial for the overall PV performance of the cells, and evaluate the self-healing properties of PSCs after proton irradiation.

3.1. Nuclear and electronic effects

The type and extent of radiation-induced damage in materials depend on the radiation type and its energy. For energetic protons, the dominant degradation mechanism in PSCs arises from non-ionizing interactions, collectively referred to as displacement damage [44,76]. In this process, incident protons transfer a portion of their energy to lattice atoms through elastic collisions, resulting in atomic displacements [27, 43]. This nuclear interaction is quantified by the NIEL, which measures the energy deposited into atomic displacements [44]. As illustrated in the upper portion of Fig. 4, such interactions initiate when the energy of an incoming proton displaces atoms from their lattice positions, forming interstitial atoms and leaving behind vacancies, together known as Frenkel pairs [31]. The displaced atoms, or primary knock-on atoms (PKAs), may carry sufficient energy to displace additional atoms, initiating a cascade of secondary displacements [27]. The vacancies act as recombination centers that enhance the non-radiative Shockley-Read-Hall (SRH) recombination, and the breakage of bonds creates localized defect states within the band gap, and their specific energy positions determine whether they function as efficient recombination centers or act as charge traps [37,87]. The minimum energy required to displace an atom is called the displacement threshold energy, with default values in SRIM simulations being 25 eV for iodine, 10 eV for hydrogen, and 28 eV for carbon, oxygen, and nitrogen [87]. However, the threshold energy values can be accurately determined with the help of molecular dynamics, which also includes the defect recombination mechanism [94]. The total displacement damage dose (DDD) due to protons is calculated by integrating the product of the differential particle flux ($\phi(E)$ and the corresponding *NIEL* values over energy. $\phi(E)$ can be obtained using particle transport simulations such as MCNP6 (Monte Carlo N-Particle Transport Code) or SPENVIS [39,48,95–97]. These nuclear interactions significantly alter the structural integrity of the PSCs, ultimately contributing to performance degradation in PSCs.

In addition to the displacement damage, energetic protons also damages the PSCs through ionization processes [44,76]. These interactions involve inelastic collisions with electrons, resulting in the excitation or ejection of electrons and the formation of electron-hole pairs [43,44]. As illustrated in the lower part of Fig. 4, an incident proton separates electrons from atoms, resulting in electron-hole pair generation within the PSC [98,99]. The electronic effects in a perovskite lattice originate from ionizing interactions, where charged particles, primarily protons, interact with the atomic electron shells, leading to progressive energy loss via multiple collisions [43]. This energy loss is characterized by the stopping power of the material expressed as dE/dx, and is referred to as specific ionization loss when dominated by electronic interactions [100]. The generated electron-hole pairs reduce the current and voltage output of the device by enhancing recombination [76]. For instance, a 20 MeV proton can produce over a thousand electron-hole pairs [27]. Ionization also disrupts the ionic and covalent bonds in perovskites, particularly within the organic components, such as C-H, C-N, and N-H bonds through radiolysis, leading to localized defect states [26,31,101–104]. Furthermore, ionization impacts the substrate by creating defects that act as optically active sites. The trapped charge carriers in these defect states absorb light via electronic transitions, giving rise to color centers that reduce glass transmittance [31,98,105–107]. Beyond these primary effects, high-energy proton interactions can also cause nuclear fragmentation of either the incident ions, the target atoms, or both, resulting in the production of secondary radiation, including lighter charged particles and neutrons [108,109]. Such irradiated samples often become temporarily radioactive and must be handled with isolation until their activity decays to safe levels [108, 110].
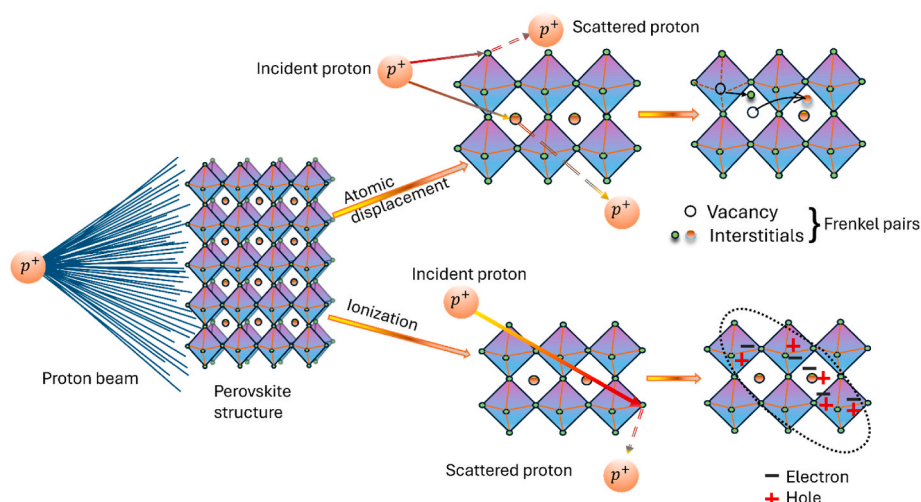

Fig. 4. Illustration of the atomic displacement and ionization of atoms due to proton irradiation.

3.2. Effect of protons on perovskite films

In the following section, the SRIM simulation and experimental observations that demonstrate how proton irradiation affects the perovskite films are detailed. SRIM simulations quantify the impact of proton irradiation on vacancy formation within the perovskite. For example, Afshari et al. reported that proton irradiation at 75 keV, 300 keV, and 1 MeV, the total vacancy counts are approximately 1.95×10^{12}, 1.66×10^{12}, and $1.82 \times 10^{12}/cm^3$, respectively. At 75 keV, most of the proton energy is dissipated within the absorber layer, whereas at higher energies the protons penetrate deeper, depositing a significant portion of their energy near the glass substrate. The SRIM vacancy-depth profiles (Fig. S1(a)–(c)) confirm this energy-dependent shift in damage localization. In the perovskite, 75 keV irradiation predominantly induces hydrogen vacancies, while at 300 keV and 1 MeV, iodide vacancies become dominant, followed by lead vacancies. This shift is attributed to the fact that higher-energy protons, being more energetic than hydrogen atoms, interact preferentially with heavier elements such as iodine and lead, rather than lighter constituents. Fig. S1(d)–(f) further reveal that although the total vacancy concentrations were matched across energies by adjusting fluences, the nature of the displaced species varies significantly, indicating a distinct defect generation mechanism driven by non-ionizing and ionizing energy loss [111].

Luo et al. evaluated the effect of 50 keV proton irradiation on MAPbI$_3$ films deposited on Fluorine-doped tin oxide (FTO) substrates over fluences ranging from 1×10^{13} to 1×10^{15} p/cm^2. Scanning electron microscopy (SEM) analysis revealed the emergence of surface holes and minor grain damage at the highest fluence (Fig. S2(a)–(c)), while X-ray diffraction (XRD) measurements indicated peak broadening and slight shifts, consistent with reduced crystallinity and partial amorphization [112]. The peak broadening observed in Fig. 5(a) resulted from the decreased crystallite size from 110 to 82.5 nm and the increased microstrain from 0.0013 to 0.00167 [112–114]. The individual contribution of the crystallite size and the microstrain to the peak broadening can be calculated using the Williamson-Hall (W-H) equation (details in supplementary file) [112,115]. Fourier transform infrared spectroscopy (FTIR) spectra in Fig. 5(b) showed a decrease in N–H and C–N bond absorption intensity, suggesting significant disruption of the organic framework. Ultraviolet–visible (UV–Vis) spectroscopy analysis in Fig. 5(c) shows a modest bandgap widening from 1.605 (before irradiation) to 1.621 eV (after 10^{15} p/cm^2) accompanied by a reduction in light absorption. This behavior is attributed to a combination of point defects and irradiation-induced microstrain, both of which contribute to an increase in hole carrier density [112,116]. In addition to these, photoluminescence (PL) quenching was observed after proton irradiation of fluence 10^{15} p/cm^2, which was attributed to the increase in the
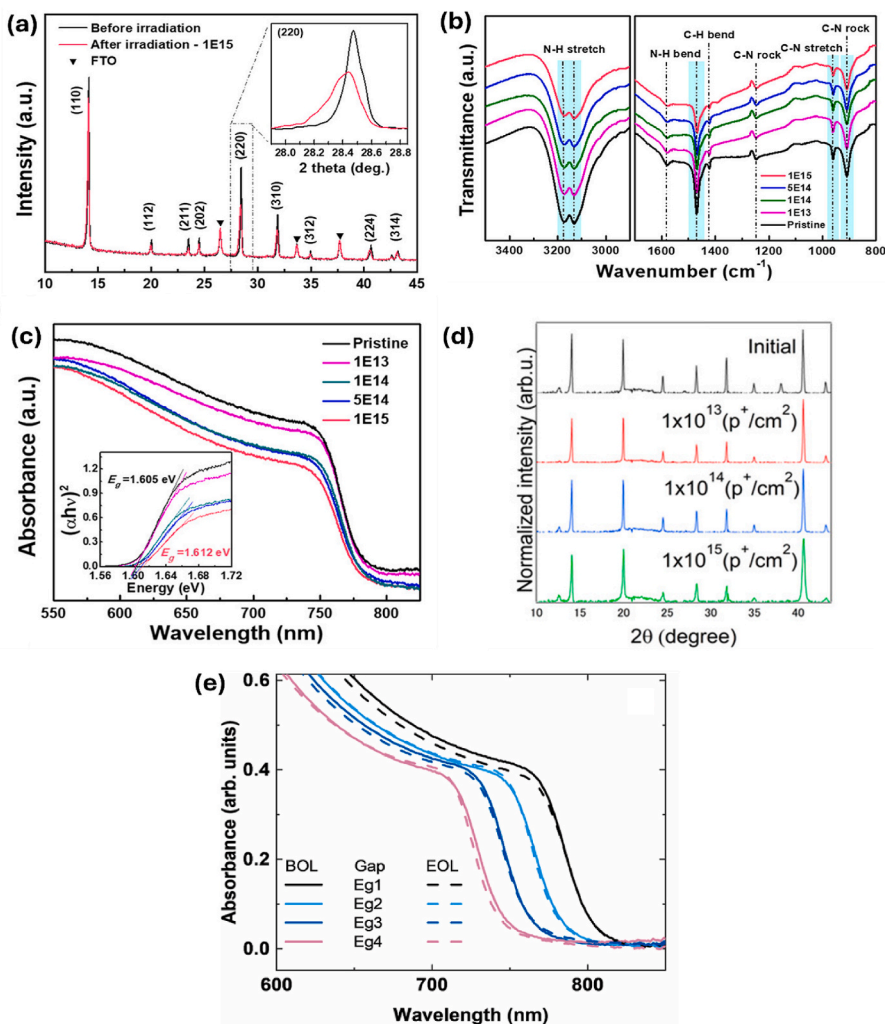

Fig. 5. *(a) XRD pattern comparison of the pristine and irradiated MAPbI$_3$ films (b)FTIR spectra for the pristine and irradiated films (c) UV–vis absorption spectra of pristine and irradiated perovskite films by 50 keV protons (adapted with permission from Ref. [112], Copyright © 2021, American Chemical Society) (d) XRD pattern comparison of the pristine and irradiated mixed cation perovskite films by 50 keV protons (adapted with permission from Ref. [120], Copyright © 2019, American Chemical Society) (e) UV–vis absorbance spectra for perovskite films before and after 1 MeV proton irradiation (adapted with permission from Ref. [121], © 2023 Elsevier B.V.).*

deep-level defect states generated by the displacement of C or H atoms in the MAPbI$_3$ lattice [112,117]. Overall, these results indicate that MAPbI3 is moderately tolerant at low fluence but suffers severe structural and electronic degradation once deep-level defects accumulate at higher fluences.

Similar to this study, a PL quench was observed after the irradiation of 170 keV protons on the mixed cation perovskite film due to the formation of deep traps and an increase in the non-radiative recombination processes [29,118,119]. The time-resolved photoluminescence (TRPL) data demonstrated a reduction in carrier lifetime from approximately 58 to 18 ns. At lower fluences, there were no significant changes observed in the XRD and SEM results. Collectively, these observations indicate that at fluences less than 10^{14} p/cm^2, MAPbI$_3$ has good proton tolerance. Due to the damage in the methylamine group, the crystallinity of the films was damaged near 1×10^{15} p/cm^2. Proton irradiation induces a degradation mechanism dominated by organic bond breakage and amorphization, which ultimately impairs charge transport and device performance [112].

Compared to the conventional MAPbI$_3$-based PSCs, Kanaya et al. demonstrated that their high-efficiency mixed-cation perovskite absorbers exhibit remarkable stability under 50 keV proton irradiation. Meanwhile, SEM (Fig. S2(d)–(f)) and XRD (Fig. 5(d)) confirmed minimal changes in grain morphology and crystal structure up to high fluences. PL and TRPL measurements provided key insights into carrier dynamics. The steady-state PL intensity didn't show any notable changes, and the slow recombination lifetime (τ_2) retained the same level of values up to 10^{14} p/cm^2. Only at a fluence of 1×10^{15} p/cm^2 was a notable reduction in carrier lifetime observed, resulting from the defects inside the grain [120]. It was reported that the mixed cation perovskite films on the substrates irradiated with 100 keV (up to 10^{14} p/cm^2), 150 keV (10^{15} p/cm^2), and 170 keV (10^{13} p/cm^2) showed no significant change in their XRD spectra [29,104,118]. Although there was no change in the crystalline structure of the perovskite, a slight increase in the surface roughness from 31 nm to 42 nm (after 10^{13} p/cm^2) was observed in the atomic force microscopy (AFM) in the perovskite for 170 keV [118]. Together, these findings highlight that mixed-cation perovskites are significantly more resilient than MAPbI$_3$, with structural integrity and carrier dynamics preserved even at high fluences, making them strong candidates for space applications.

Costa et al. employed four I/Br ratios (Eg1:91/9, Eg2:83/17, Eg3:75/25, and Eg4:67/33) to adjust the perovskite bandgap, aiming for optimal efficiency and radiation stability. They irradiated the cells using 1 MeV protons at 5×10^{14} p/cm^2. Fig. 5(e) shows the UV–Vis absorbance spectra for the perovskite materials at the BOL (beginning-of-life) and EOL corresponding to the conditions before and after proton irradiation. It showed that the perovskite films with higher iodine content exhibited greater absorbance loss, attributed to the migration of iodine species, including volatile I$_2$, through the device layers [107,119,121,122]. This demonstrates that halide composition strongly influences radiation stability, with partial substitution of iodine by bromine mitigating halide migration and enhancing tolerance.

As the energy of the proton beam further increased, the degradation of the perovskite films worsened. Xue et al. examined a mixed-cation perovskite film deposited on SnO$_2$/FTO/glass via spin-coating and annealing. 2 MeV proton irradiation up to 2.2×10^{15} p/cm^2 caused severe decomposition, as XRD showed increased PbI$_2$ peaks. PL intensity decreased at high fluence, signaling disordered emission. These effects arise from electronic energy deposition causing radiolysis, breaking organic bonds, and generating gases that degrade the film [104]. Under 10 MeV proton irradiation at fluences of 10^{12} to 10^{14} p/cm^2, perovskite films exhibited void formation, surface ablation, and increased roughness, while PL intensity and carrier lifetime were reduced. These results indicate that high-energy proton bombardment causes both mechanical damage and optoelectronic property degradation [108]. Similarly, 68 MeV protons cause a decrease in the steady-state PL intensity [27]. These studies highlight a superior radiation tolerance of the mixed-cation perovskites at low-energy low-fluence compared to typical MAPbI$_3$ layers, which tend to show more significant degradation under similar conditions.

3.3. Proton resilience of substrates and electrodes

In this section, the effects of proton irradiation on substrates are investigated by examining changes in their structural, optical, and chemical properties, with a focus on detailing the degradation mechanisms and the resilience of the materials under proton beam exposure. In addition, the electrode layers are evaluated for changes in transparency and sheet resistivity to understand their functional stability under irradiation.

3.3.1. Flexible substrates

The analysis begins with flexible substrates, which are widely used for lightweight, portable, and wearable devices due to their mechanical flexibility and compatibility with low-temperature processing [31]. Čermák et al. examined the effects of a 3 MeV proton beam on PET foil. AFM images in Fig. S3 show reduced roughness, but they reported that the film turned yellow and became mechanically bent with chemical degradation, marked by additional hydroxyl, carboxylic, and silanol groups [123]. Saito et al. experimented to find the radiation resistance of different flexible substrates. They irradiated various polymer films, including aromatic polyimide (PI), PET, and PEN, with 2.2 MeV protons up to a fluence of 2.1×10^{16} p/cm^2. FTIR spectra were recorded to check the atomic composition and structure after irradiation, which can be seen in Fig. 6(a). A drop in intensity of the absorption band of the C-O and C=O group bonds was observed for both PET and PEN films after irradiation, suggesting degradation after proton irradiation. On the other hand, there was no significant change in the absorption intensity of the PI film [124]. PI films usually display a strong absorption in the UV and short wavelength regions but show coloration ranging from dark yellow to reddish brown at the longer wavelengths, making them a less favorable choice as substrates for the PSCs [125,126]. Malinkiewicz et al. irradiated the PET films with 3 MeV proton beams and noticed that there was no significant change in the transmittance of the PET substrate at 440 nm after irradiation up to 3×10^{12} p/cm^2 and a slight decrease after that, as illustrated in Fig. 6(b). There was no formation of active sites in the PET after 3 MeV irradiation [31]. The literature is inconsistent regarding the proton resilience of flexible substrates, with different studies offering conflicting findings. This inconsistency could be attributed to variations in experimental conditions, such as proton fluence, beam energy, or sample preparation methods. Overall, these results indicate that while PET and PEN films undergo chemical and optical degradation at high fluences, PI retains structural robustness but suffers from coloration that reduces optical suitability. Thus, no flexible substrate currently offers an ideal balance of radiation resistance and transparency, and further optimization is required.

3.3.2. Rigid substrates

Following the analysis of flexible substrates, the study now turns to rigid substrates, which offer superior thermal and mechanical stability under proton irradiation [127]. Along with the flexible substrate, Čermák et al. examined the effects of a 3 MeV proton beam on rigid substrates, including Eagle XG glass and soda lime glass. Using AFM (Fig. S3) and spectroscopic methods, they found that Eagle XG glass exhibited minimal changes, whereas soda lime glass developed scratches and cracks due to tensile stress [123]. Some studies reported the formation of color centers in glass substrates after proton irradiation [105,106]. When glass was irradiated with 2 MeV up to a fluence of 2.2×10^{15} p/cm^2, it loses a small amount of its transmittance, but the higher the proton energy, the greater the transmission loss [104].

Beyond these experimental observations, SRIM provides insights into the shielding role of substrates. For instance, 150 keV protons incident from the quartz substrate side lose all their energy within the first 0.23
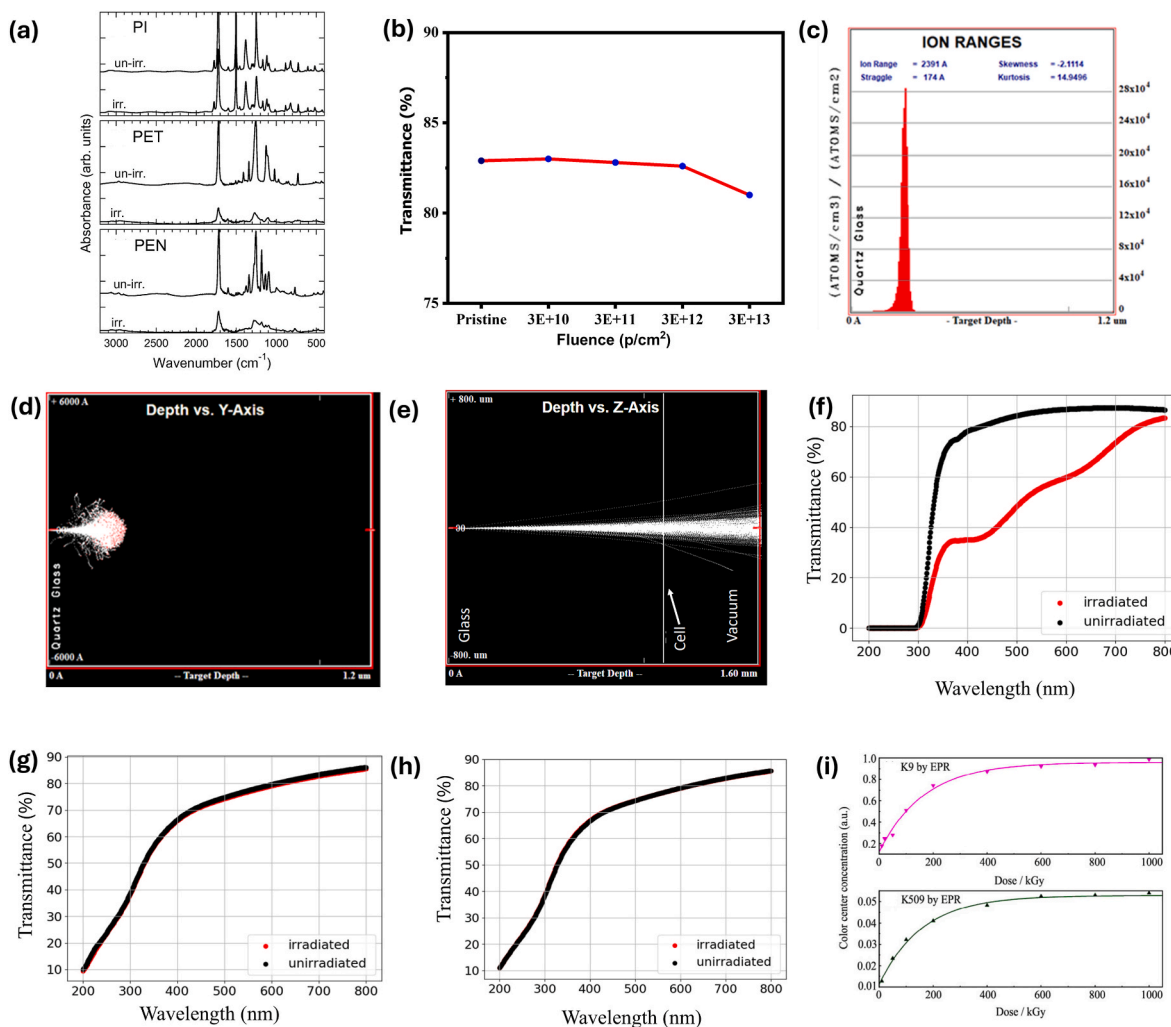
Fig. 6. (a) Comparison of FTIR spectra of PI, PET, and PEN before and after irradiation with 2.2 MeV protons (adapted with permission from Ref. [124], Copyright © 2010 Elsevier B.V.), (b) the transmittance of the PET foil as a function of fluence for 3 MeV proton [31](c) ion range histograms for 150 keV protons are incident from the substrate side, (d) 150 keV proton distribution inside the PSC when incident from the substrate (adapted with permission from reference [29],© 2019 WILEY-VCH Verlag GmbH & Co. KGaA, Weinheim) (e) 15 MeV proton distribution inside the PSC when incident through the substrate (adapted with permission from Ref. [108], © 2024 Wiley-VCH GmbH), transmission spectra of (f) soda-lime glass, (g) fused quartz glass, (h) fused silica glass before and after 17.5 MeV proton beam irradiation (Adapted under the terms of the Creative Commons Attribution 4.0 license from Ref. [132], published by IOP Publishing Ltd on behalf of Sissa Medialab, © 2021 CERN), (i) color center concentration in cerium-free glass (K9) and cerium-doped glass (K509) as a function of gamma dose according to EPR spectra (adapted with permission from Ref. [133], Copyright © 2014 The Chinese Society of Rare Earths. Published by Elsevier B.V). (For interpretation of the references to color in this figure legend, the reader is referred to the Web version of this article.)

μm of the 1 mm-thick substrate, never reaching electrically active components (Fig. 6(c) and (d)). Similarly, 250 keV protons penetrate glass only about 2.1 μm, underscoring that the substrates act as efficient shields against low-energy irradiation [29,128]. At higher energies, however, the shielding effect diminishes. SRIM simulations indicate that 15 MeV protons can fully traverse a 1.1 mm glass substrate, reaching the absorber and adjacent functional layers (Fig. 6(e)). This demonstrates that while glass effectively blocks low-energy irradiation, it becomes increasingly transparent to protons at MeV energies, enabling deeper damage pathways [108].

Unlike glass, quartz does not darken after irradiation and has better radiation resistance than glass [29,85,129,130]. After exposure to the proton beam up to the fluence of 10^{14} p/cm², the quartz substrate exhibited no noticeable change in its transmittance [131]. Supporting this claim, Oliveira et al. compared the optical transmittance spectra for various substrates before and after irradiation with 17.5 MeV protons. Fig. 6(f)–(h) shows the optical transmittance spectra of the soda-lime glass, fused quartz glass, and fused silica glass, respectively. This study showed that fused silica glass exhibits the highest resistance to proton

irradiation, with only a 0.4 % decrease in optical transmission and no visible scintillation or color center formation. Fused quartz also demonstrates good radiation tolerance, with a minor 1 % transmission loss, though it does exhibit some scintillation. In contrast, soda-lime glass shows poor proton resistance, suffering a 45 % reduction in transmission and clear radiation-induced discoloration. These results highlight fused silica as the most suitable material for applications requiring stable optical properties under irradiation [132]. Fig. 6(i) shows the color center concentration in cerium-free glass (K9) and cerium-doped glass (K509) as a function of gamma dose according to electron paramagnetic resonance (EPR) spectra. This illustrates that cerium-doped glass forms significantly fewer radiation-induced color centers compared to the cerium-free glass as the gamma dose increases. This reduced defect formation highlights the role of cerium in enhancing radiation resistance by suppressing both electron- and hole-trapped centers [133]. Although the study by Fu et al. focused on gamma irradiation, their findings demonstrated a substantial reduction in color center formation in cerium-doped glass compared to cerium-free counterparts. Given that PSCs generally exhibit greater resilience to low-energy protons than to

γ-rays, it is highly probable that cerium-containing glasses would show even better radiation tolerance under proton irradiation, further supporting their suitability for space applications [128,133]. Some studies have explored the use of steel as an alternative to glass and flexible substrates [134,135]. However, there remains a lack of comprehensive testing to evaluate its resistance to proton irradiation. In conclusion, rigid substrates such as quartz and fused silica clearly outperform soda-lime and conventional glass in terms of proton resistance, with cerium-doped compositions offering additional protection against defect formation. These results underscore that careful substrate selection can significantly improve optical stability and shielding efficiency in PSCs exposed to radiation.

3.3.3. TCO

Following the discussion on substrates, the role of TCOs becomes equally critical, as they serve not only as front electrodes but also as optical windows, influencing both electrical and optical performance of optoelectronic devices under irradiation. FTO, a commonly employed TCO, exhibits promising attributes such as ~80 % optical transmittance above 300 nm and an initial electrical resistivity of 12.7 $\Omega \cdot cm$. Upon exposure to 7 MeV protons, the resistivity decreased slightly to 11.5 $\Omega \cdot cm$ at a fluence of 1×10^{15} ions/cm^2, suggesting defect-induced enhancement of free carrier density. However, at higher fluences, particularly 1×10^{16} ions/cm^2, resistivity sharply increased to 27.0 $\Omega \cdot cm$, indicating the formation of deep-level trapping centers that hinder carrier transport. Concurrently, optical transmittance degraded progressively with increasing fluence, reflecting enhanced light absorption due to defect-related color centers. These results suggest that while FTO maintains functional transparency and conductivity under low-dose irradiation, its performance as a TCO is significantly compromised at high proton fluences, raising concerns about its suitability in space or nuclear radiation environments [136]. ITO is one of the most widely used TCO, demonstrating high resilience under 3 MeV proton irradiation at fluences up to 10^{15} p/cm^2. The sheet resistance remained stable at ~10 Ω/sq on glass and ~60 Ω/sq on PET, with no observable morphological degradation. Optical absorbance showed only a slight increase, mainly in ITO/PET, which was attributed to PET degradation rather than the ITO layer itself. The work function shift calculated using
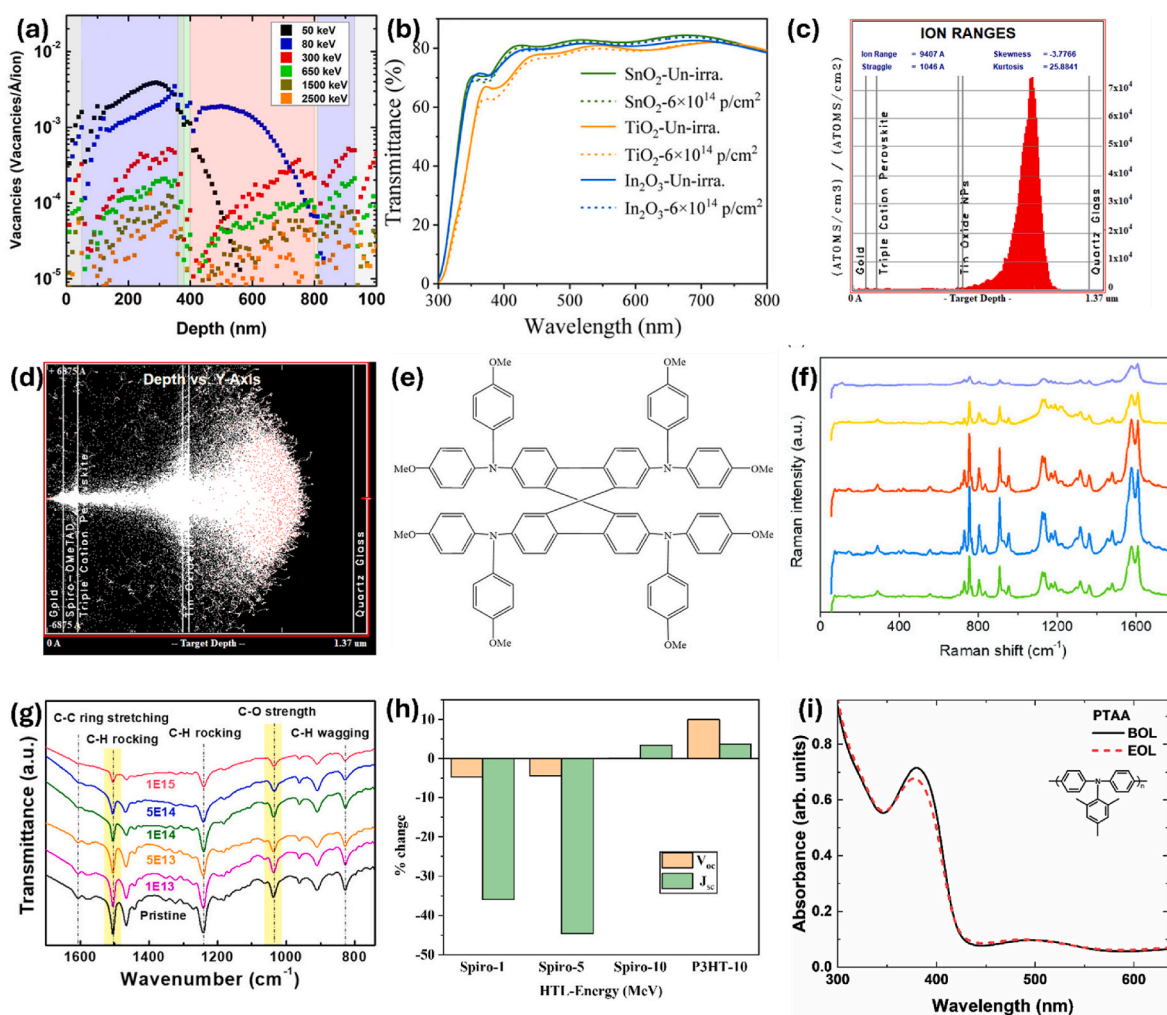

Fig. 7. (a) SRIM calculations of vacancies as a function of depth (adapted with permission from Ref. [43], Copyright © 2021, American Chemical Society) (b) Optical transmittance spectra of glass/FTO/ETL before and after proton irradiation (adapted with permission from Ref. [128], Copyright © 2023, American Chemical Society) (c) ion range histograms for 150 keV protons incident from the substrate side, (d)150 keV proton distribution inside the PSC when incident from the top electrode (adapted with permission from Ref. [29], © 2019 WILEY-VCH Verlag GmbH & Co. KGaA, Weinheim), (e) Structure of spiro-OMeTAD [163], (f) Raman spectra of the PSC probing the spiro-OMeTAD measured between 0 and 1800 cm^{-1} (adapted with permission from Ref. [29], © 2019 WILEY-VCH Verlag GmbH & Co. KGaA, Weinheim), (g) FTIR spectra of spiro-OMeTAD films before and after irradiation (adapted with permission from Ref. [112], Copyright © 2021, American Chemical Society), (h) Comparison of percentage change of V_{oc} and J_{sc} for devices with spiro-OMeTAD and P3HT as its HTL for different incident proton energy [37], (i) UV–visible Absorbance spectra of PTAA before and after irradiation of 1 MeV proton at 5×10^{14} p/cm^2 (adapted with permission from Ref. [121], © 2023 Elsevier B.V.).

Kelvin Probe Force Microscopy (KPFM), remained within $\pm$ 60 meV, indicating a negligible impact on its electronic properties. These findings confirm the suitability of ITO as a radiation-tolerant TCO for space photovoltaics [123].

In contrast to the experimental findings, SRIM simulations revealed vacancy formation in the ITO layer under proton irradiation. Irradiation with 100 keV to 1 MeV protons produced a significant number of indium and oxygen vacancies, with their distribution strongly dependent on energy [118]. Collision event profiles further showed vacancy generation within both the ITO and perovskite layers (Fig. 7 (a)) [43]. However, the absence of macroscopic changes in experiments reflects the limitations of SRIM, which does not account for defect recombination, dynamic annealing, or complex chemical processes.

Following the discussion on commonly used TCO; ITO and FTO, another potential candidate for transparent conducting applications is indium-doped zinc oxide (IZO). Under 5 MeV proton irradiation, IZO shows a non-monotonic response. At low to moderate fluences (up to 10^{13} p/cm^2), the resistivity increases significantly, attributed to defect-induced carrier trapping and lattice disorder. However, at higher fluences (10^{14}-10^{15} p/cm^2), the resistivity recovers to values close to the unirradiated state, due to dynamic annealing and the formation of oxygen vacancies that act as shallow donors [137]. AZO has gained attention as a cost-effective and abundant alternative for space applications. Barbé et al. investigated the radiation response of PSCs incorporating AZO as the TCO under 150 keV proton irradiation. Their results showed that AZO maintained stable optical properties up to a fluence of 10^{15} p/cm^2, with no measurable change in transmittance or structural degradation, as confirmed by XRD and UV–Vis analysis [29]. However, under irradiation of 226.5 MeV protons, which are less likely to be found in space, AZO exhibited a more complex response. Following exposure to 226.5 MeV protons at a fluence of 10^{11} p/cm^2, sheet resistance decreased from 302.5 Ω/sq to 202.3 Ω/sq, suggesting improved conductivity, likely due to the formation of oxygen vacancies. However, X-ray photoelectron spectroscopy (XPS) revealed shifts in binding energies—e.g., Zn 2p from 1021.3 eV to 1021.5 eV and Al 2p from 73.6 eV to 73.8 eV—indicating increased surface resistance. Transmittance dropped slightly in the 400–630 nm range, while ellipsometry showed a rise in extinction coefficient beyond 1000 nm, consistent with enhanced free carrier absorption. Despite improved conductivity, these surface-level changes and reduced optical clarity suggest limited stability of AZO in a harsh radiation environment [138]. To conclude, the radiation tolerance of TCOs varies significantly with both material type and proton energy. ITO showed an excellent stability compared to FTO, while AZO and IZO exhibited mixed behavior depending on fluence and energy.

3.3.4. Top electrode

While the TCO layer facilitates efficient charge collection and light transmission, the top electrode is vital for circuit completion and overall device stability. Silver is a widely used electrode due to its high conductivity and low cost; however, its interaction with halide perovskites raises concerns. When deposited on iodide-based perovskites, silver forms discontinuous particles that react with iodide to produce AgI, triggering further degradation of the perovskite through cation loss and lead oxide formation. Bromide-only perovskites exhibit slower reactions, though degradation still occurs. The process is primarily driven by volatile halide byproducts like HI and I$_2$, which can corrode silver even without direct contact. These findings highlight the vulnerability of silver electrodes in real devices, especially in the presence of pinholes or imperfect buffer layers [139]. One potential approach to mitigate this degradation is to replace silver with gold, which is more resistant to halide-induced reactions; however, the high material cost of gold poses a significant barrier to its large-scale industrial adoption [140]. Although this study does not address proton irradiation, the chemical pathways outlined here suggest that similar or even worse degradation could occur under proton exposure, making robust encapsulation essential for

long-term stability [139]. Moreover, SRIM-based studies indicate that silver electrodes also influence proton interaction pathways. Compared to glass, the higher density of silver causes high-energy protons to undergo predominantly ionizing (electronic) interactions rather than nuclear collisions [87]. This implies that while silver ensures conductivity, it may also alter the radiation response of the device, making encapsulation and electrode material selection doubly critical in proton-rich environments.

Unlike conventional metal electrodes like silver and gold, which are typically thin and susceptible to chemical degradation or diffusion, carbon-based electrodes offer superior chemical stability and mechanical robustness. In particular, mesoporous carbon electrodes have shown exceptional resistance to proton irradiation. Screen-printed perovskite solar cells with a ~12 μm thick carbon layer maintained stable performance even after exposure to 150 keV protons at fluences up to 1×10^{15} p/cm^2. Key performance parameters such as PCE, V_{oc}, and J_{sc} remained virtually unchanged. Optical and structural analyses confirmed no significant damage to either the perovskite or carbon layers. This durability is largely attributed to the thickness of the carbon layer, which effectively shields the active region from proton penetration. These findings establish carbon electrodes as a reliable choice, offering both conductivity and built-in radiation protection for space-focused solar technologies [141].

3.4. Proton irradiation-induced damage in the charge transport layer

In this section, the impact of proton irradiation on the CTLs in PSCs is examined. The focus is placed on how irradiation alters their structural integrity, chemical composition, and PV performance. The CTLs are present on either side of the perovskite in both p-i-n and n-i-p structures. Protons, regardless of their energy, lose most of their energy within the CTLs and electrodes. This energy deposition leads to a higher concentration of defects, such as vacancies and ionized atoms, and increased phonon activity at the interface between the perovskite and the CTLs [100]. This section investigates the effects of proton irradiation on both organic and inorganic CTLs.

3.4.1. Metal oxide HTLs

Some commonly used metal oxide HTLs as NiO$_x$, MoO$_x$, and CuO. There is a lack of studies that directly assess the proton resistance of metal oxide HTLs alone. However, several works have used materials like NiO$_x$ in PSCs and tested the full devices under proton irradiation. In the study by Colenbrander et al., PSCs employing NiO$_x$ as the HTL were fabricated using a sputtered NiO$_x$ thin film, followed by a PTAA interlayer and a mixed-halide perovskite absorber. These devices were subjected to low-energy proton irradiation at 75 keV with fluences up to 1.73×10^{14} p/cm^2 to evaluate their suitability for deep space applications. Notably, even after exposure to a fluence of 4.35×10^{13} p/cm^2, the devices retained a substantial portion of their original efficiency when operated under simulated outer planetary conditions, including temperatures as low as −140 °C and solar intensities representative of 19.2 AU [48]. The sustained device performance suggests that these layers are likely tolerant to proton exposure, though their individual behavior remains unverified.

3.4.2. Metal oxide ETLs

To understand the resistance of ETLs against proton experimentally, Liu et al. irradiated the glass/FTO/ETL (ETL: SnO$_2$, TiO$_2$, and In$_2$O$_3$) with 250 keV protons to fluence 6×10^{14} p/cm^2. Fig. 7(b) shows the transmittance spectra of the glass/FTO/ETL before and after proton irradiation for all three ETLs. The radiation causes minimal alterations in light transmission through the transparent glass/FTO/ETL substrates. The decrease in transmission across the spectrum from 300 to 800 nm is negligible, at less than 1.5 %, primarily due to the irradiation-induced tinting of the glasses. The ETLs exhibited only minor degradation, with their resistance increasing by merely 15–19 %. Therefore, it can be

concluded that the ETL is not responsible for the degradation of the PSCs under proton irradiation [128]. These observations align with the findings of Barbé et al., whose SRIM simulations (Fig. 7(c) and (d)) showed that a significant fraction of low-energy (150 keV) protons stop within the SnO_2 ETL. Despite this, experimental results from the same study revealed that the observed decrease in short-circuit current at 150 keV was not due to ETL degradation but instead linked to interfacial deterioration of the Spiro-OMeTAD HTL, which will be discussed in the next section [29]. Taken together, these results demonstrate that metal oxide ETLs such as SnO_2 remain comparatively robust under proton exposure.

3.4.3. Organic HTLs

Many literatures using an organic HTL, report that HTL was the site of reduced carrier extraction and interface degradation [87,142,143]. 2, 2′,7,7′-tetrakis-(N,N-di-4-methoxyphenylamino)-9,9′-spirobifluorene, also called spiro-OMeTAD is the most commonly used HTL in the PSCs, and its structure is given in Fig. 7(e) [104].To better understand the comparison between the degradation in perovskite, ETL, and HTL, SRIM was used to see the vacancies generated in all three layers. SnO_2 as the ETL, $MAPbI_3$ as the perovskite layer, and spiro-OMeTAD as the HTL were used in simulations. The results show that 0.11 % vacancies were generated in SnO_2, which is negligible compared to 3.5 % in $MAPbI_3$ and 19.8 % in the spiro-OMeTAD [112]. Following this, Luo et al. simulated the vacancy concentration after the irradiation of a 50 keV proton beam on the PSC, which resulted in spiro-OMeTAD producing a vacancy ratio of 7.6 %, which is considered to cause serious irradiation damage for organic molecules [112,144].

Barbé et al. irradiated a 150 keV proton beam on the PSC with the structure Quartz/AZO/SnO_2/$Cs_{0.05}(MA_{0.17}FA_{0.83})_{0.95}Pb(I_{0.83}Br_{0.17})_3$/spiro-OMeTAD/Au and noticed that there was no significant change in the crystalline structure of the perovskite films. Contradicting this, they reported a significant drop in the PV parameters for the fluence 10^{14} p/cm^2, which could be due to a damaged transport layer. This means that either the SnO_2 layer or the spiro-OMeTAD interlayers were compromised [29,145,146]. Due to the inorganic nature of SnO_2, it has good thermal stability and irradiation resistance, and it is incapable of producing strong PL or Raman signals [112,147,148]. Therefore, Barbé et al. recorded Raman spectra of the spiro-OMeTAD and are shown in Fig. 7(f).The Raman spectra remained unchanged at fluences up to 10^{13} p/cm^2. The peak intensity started to decline after irradiation of 10^{14} p/cm^2 and further deteriorated at 10^{15} p/cm^2. TPV decay showed a faster time constant, which was attributed to the interfacial recombination in the perovskite/HTL interface. It was concluded that the degradation in the spiro-OMeTAD was responsible for the decreased PV parameters [29]. This demonstrates that the perovskite/organic HTL interface is a critical weak point under irradiation stress.

Xue et al. reported that the drop in J_{sc} observed after proton irradiation was primarily due to the poor structural stability of the spiro-OMeTAD layer. Decomposition of the perovskite generates gaseous byproducts such as HI, HCN, and NH_3 that can diffuse into the spiro-OMeTAD, leading to its volume deformation [104,149]. SEM images revealed an increased surface roughness with cauliflower-like features and partial exfoliation of the Au electrode, indicating that strain from the deformed spiro-OMeTAD contributes significantly to device degradation [104]. As seen in Fig. 7(e) the methyl group (CH_3) is positioned in the outermost part of the spiro-OMeTAD structure, and it is more prone to radiation than the other molecules [112,150,151]. Fig. 7(g) shows the FTIR spectra of the proton-irradiated spiro-OMeTAD films on the perovskite layers. The intensity of the absorption peaks of the C-H in the methyl group and the C-O attached to it decreases as the proton fluence increases. Luo et al. concluded that the molecular bonds of the spiro-OMeTAD break when it is irradiated with a proton beam and lose its charge extraction properties [112]. Recycling the layer is an effective strategy to mitigate degradation, and optimizing the Lithium bis(trifluoromethanesulfonyl)imide (LiTFSI) doping concentration is another

viable option [152]. Thus, both chemical decomposition and interfacial strain contribute to the poor radiation tolerance of spiro-OMeTAD. However, employing silver or gold electrodes for recycling would be cost-prohibitive, and noble metals can even accelerate perovskite degradation by influencing their electrical properties through electrochemical doping [131,139,153]. Consequently, using carbon electrodes could offer a more economical and stable alternative [131].

Liu et al. investigated PSCs employing a LiTFSI, FK209, and 4-tert-Butylpyridine (tBP) doped spiro-OMeTAD HTL along with various ETLs (SnO_2, TiO_2, and In_2O_3) under 250 keV proton irradiation. They observed that the additives in spiro-OMeTAD, which create spiro-$OMeTAD^+$ cations and boost Raman intensity, are de-doped during irradiation at a fluence of 3×10^{14} p/cm^2. This was evidenced by a decrease and broadening of the Raman peaks until they resembled those of undoped spiro-OMeTAD [128]. Since Li-TFSI is known to actively migrate across the device stack, proton exposure likely displaces Li-TFSI, further contributing to the de-doping of spiro-OMeTAD [154–156]. Hence, the common practice of heavy doping to enhance conductivity may in fact exacerbate instability under proton exposure.

Due to the poor radiation stability of spiro-OMeTAD and the limited benefits of doping, exploring alternative hole transport materials becomes essential. Martínez et al. created two n-i-p $MAPbI_3$ devices with spiro-OMeTAD and Poly(3-hexylthiophene-2,5-diyl) (P3HT) as the HTLs. Fig. 7(h) shows the comparison of the PV parameters (J_{sc} and V_{oc}) for both devices. Spiro-1 represents devices irradiated with 1 MeV protons, and a similar notation is used for 5 and 10 MeV. The P3HT devices were irradiated with 10 MeV protons. The devices with spiro-OMeTAD showed a significant decrease in the PV parameters for proton energies 1 MeV and 5 MeV and a slight increase for 10 MeV. Since the low-energy protons have a higher probability of collisions than high-energy protons due to the increased Coulomb cross-section, the 1 MeV and 5 MeV protons produce more degradation in the PV parameters than the 10 MeV protons. Unlike spiro-OMeTAD, which showed poor proton resistance, P3HT devices showed improved PV parameters after 10 MeV proton irradiation. The V_{oc} increased by 10 %, while J_{sc} showed a slight increase together, resulting in a 42.1 % increase in PCE. This improvement was attributed to proton-induced defect healing in the P3HT layer and a potential doping effect, which improved hole extraction and reduced recombination [37]. This suggests that alternative polymers such as P3HT may provide not only higher radiation tolerance but also opportunities for radiation-assisted performance enhancement.

To explore the radiation resistance of Poly[bis(4-phenyl)(2,4,6-trimethylphenyl)amine] (PTAA) as an HTL, Costa et al. irradiated glass/PTAA with 250 keV protons and found that they are vulnerable to radiation. Fig. 7(i) shows the UV–visible absorbance of the control and the irradiated substrates. They observed a notable reduction in UV–visible absorbance near 380 nm, suggesting chain scission, along with an increase in contact resistivity from TLM measurements. These changes in PTAA correlated with significant declines in J_{sc} and FF. The recovery of device performance after depositing new PTAA layers on irradiated perovskite films confirmed that PTAA degradation was a key factor in overall performance loss [121]. Thus, while PTAA avoids some drawbacks of spiro-OMeTAD, it still suffers from bond scission and conductivity loss, limiting its long-term applicability in space environments.

These result raises concerns regarding the long-term stability of spiro-OMeTAD in space environments, while alternative HTLs such as P3HT have yet to demonstrate comparable efficiency [128]. The usage of inappropriate HTL in a solar cell can reduce the proton damage threshold of the device [112]. These results suggest that further research and optimization are required to develop a robust and high-performing HTL for durable PSC designs.

3.4.4. Organic ETLs

There are very few studies that specifically evaluate the proton irradiation resistance of organic ETLs. However, the radiation durability of fullerene-based ETLs has been explored using [6,

6]-Phenyl-C$_{60}$-butyric acid methyl ester (PC$_{60}$BM) under γ-ray exposure. Pristine PC$_{60}$BM films exhibited a notable increase in conductivity, likely due to radiation-induced doping, even though no accumulation of stable radicals was detected by Electron Spin Resonance (ESR) analysis. Despite this, degradation in device performance was observed, suggesting the formation of trap states. When blended with the donor polymer Poly[N-9′-heptadecanyl-2,7-carbazole-alt-5,5-(4′,7′-di-2-thienyl-2′,1′,3′-benzothiadiazole)] (PCDTBT), PC$_{60}$BM demonstrated remarkable stability, with solar cells retaining about 90 % of their initial efficiency after 6500 Gy. In contrast, devices incorporating Poly[N-9′-heptadecanyl-2,7-carbazole-alt-5,5′-(4,7-bis(5′-hexylthien-2′-yl)-2,1,3-benzothiadiazole-bithiophene)] (PCDTTBTBTT) exhibited greater radiation sensitivity, losing over 50 % of efficiency at just 200–500 Gy. These results suggest that although PC$_{60}$BM alone is vulnerable to radiation-induced defects, its stability can be significantly improved through blending with more robust donor polymers [157].

Since the focus of this review is on proton irradiation, it is relevant to highlight a study that investigates the behavior of fullerene-based ETLs, specifically PC$_{61}$BM, under exposure to 68 MeV protons at a fluence of 1.02×10^{13} p/cm^2. Brus et al. used PC$_{61}$BM as the ETL in the devices and reported that the dielectric constant of the PC$_{61}$BM layer remained unaffected by the irradiation. Additionally, no signs of degradation or increase in resistive components were observed in the equivalent circuit of the device. These findings suggest that PC$_{61}$BM retained its electrical stability under proton exposure, indicating promising radiation durability [26].

While significant research has focused on tailoring ETLs and HTLs, whether organic or metal oxide, to improve device performance and stability under radiation, another proposed strategy is to eliminate these layers altogether. Although several studies have demonstrated promising efficiency and stability improvements in ETL-free and HTL-free devices, their radiation tolerance has not yet been systematically evaluated [158,159]. As noted by Luo et al., simplifying device structures without transport layers is expected to achieve better irradiation stability, but this remains a research gap that warrants future investigation [112,160–162].

3.5. Device-level degradation under proton irradiation

In the previous sections, the effects of proton irradiation on the various layers of the PSCs were outlined. In this section, the focus is placed on experiments and simulations conducted on the complete device. As discussed in Section 3.1, the proton energy critically governs the interaction mechanisms within the perovskite lattice. Increasing the energy of incident protons shifts their interaction within the absorber lattice from predominantly nuclear to primarily electronic effects [43,
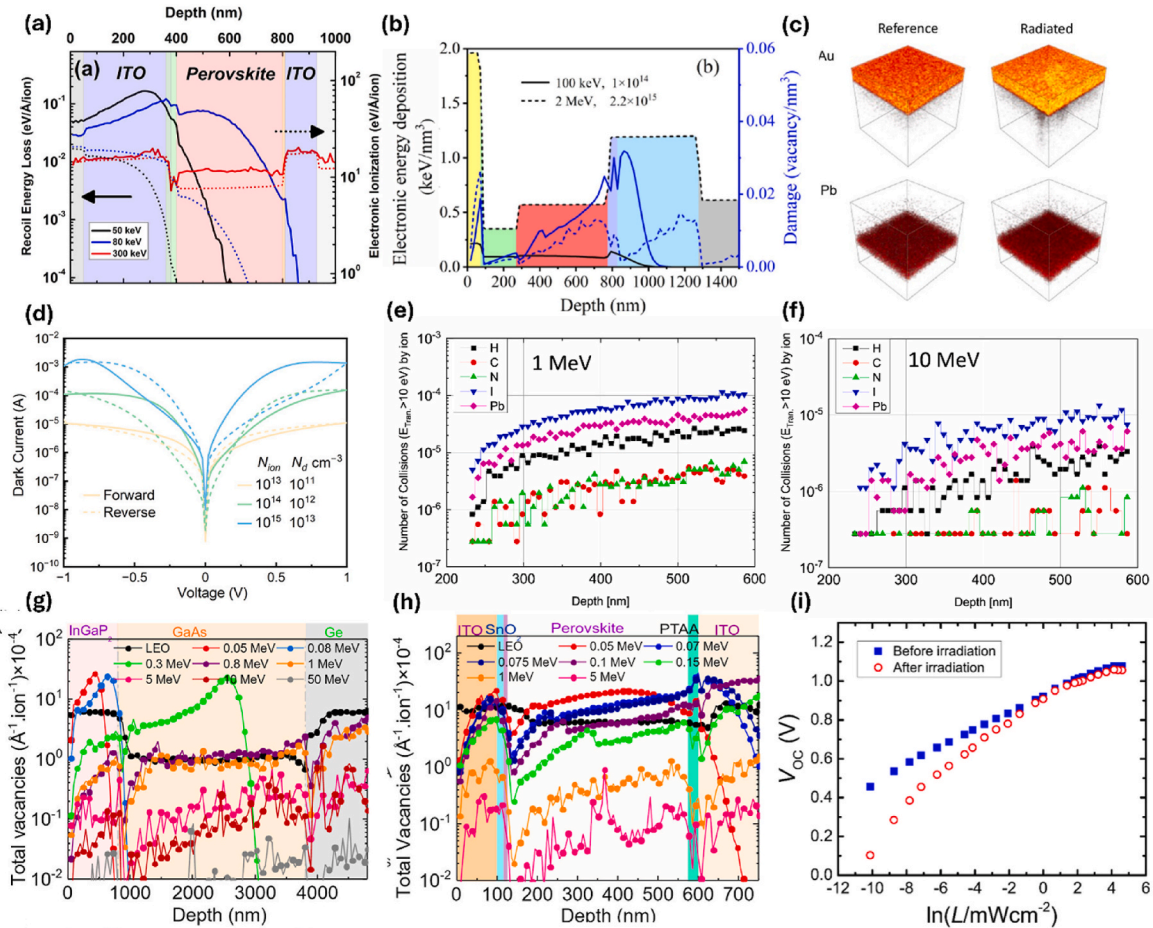

Fig. 8. (a) SRIM calculations of 50 keV Recoil Energy Loss and Electronic Ionization (adapted with permission from Ref. [43], Copyright © 2021, American Chemical Society), (b) electronic energy deposition and atomic displacements per volume in PSCs for 100 keV and 2 MeV (adapted with permission from Ref. [104], © 2022 Elsevier B.V.), (c) ToF-SIMS 3D mapping results for Au and Pb atoms (adapted from with permission from Ref. [108], © 2024 Wiley-VCH GmbH), (d) forward and reverse scans of dark I−V curves with different ion densities and doping densities (adapted with permission from Ref. [131], Copyright © 2024, American Chemical Society), distribution of C, H, N, Pb and I atom vacancies in the perovskite layer for (e) 1 MeV proton, (f) 10 MeV proton (adapted with permission from Ref. [37], © 2022 Elsevier B.V.), total damage profiles produced by various proton energies irradiating the (g) III-V solar cell, (h) PSC (adapted with permission from Ref. [90], Copyright © 2025, American Chemical Society) (i) The dependence of V_{oc} on the light intensity for devices before and after irradiation (adapted from Ref. [89], Copyright © 2024, The Authors)).

87]. Hence, the recoil energy loss will be less than electronic ionization for higher proton energies. Fig. 8(a) supports this observation, showing that the recoil energy loss at 300 keV is lower than at 80 keV and 50 keV, whereas the electronic ionization increases with energy. The collision events profile in Fig. 8(a) indicates that the interactions are primarily elastic with the nuclei, resembling hard sphere collisions. This behavior results in significant recoil energy loss, which contributes to an increased number of atomic displacements, commonly referred to as vacancies. Fig. 8(b) shows the electronic energy deposition and vacancy generation in PSCs subjected to irradiation with 100 keV protons at a fluence of 1×10^{14} p/cm^2 and 2 MeV protons at a fluence of 2.2×10^{15} p/cm^2. SRIM results demonstrated that, for 100 keV protons, the perovskite film experiences an electronic stopping power of approximately 100 eV/nm and a nuclear stopping power of about 0.07 eV/nm. By contrast, 2 MeV protons exhibit much lower values, around 25 eV/nm for electronic and 0.004 eV/nm for nuclear stopping. These results highlight the critical role of electronic energy loss in the degradation of perovskite films [104]. Thus, device degradation is closely tied to the balance between nuclear and electronic energy loss, with higher proton energies shifting the mechanism toward ionization-driven damage.

Fig. 8(c) shows the time-of-flight secondary ion mass spectrometry (ToF-SIMS) 3D mapping results for Au and Pb atoms as demonstrated by Nguyen et al. They reported that PSCs irradiated with 140 keV protons up to a fluence of 1×10^{12} p/cm^2 show significant migration of gold atoms from the top electrode into the underlying spiro-OMeTAD and perovskite layers. This displacement can result in widespread contamination of the device and further degradation due to subsequent chemical reactions, in addition to the radiation-induced defects. Similarly, the migration of lead ions into the SnO$_2$ layer has also been observed. These observations emphasize that radiation-induced ion migration, particularly of electrode and absorber constituents, is an additional failure pathway beyond simple vacancy generation.

In their study on complete devices, Huang et al. monitored dark I–V curves in situ (Fig. 8(d)) during 1.8 MeV proton irradiation up to a fluence of 1×10^{14} p/cm^2. They observed that the average dark current at $\pm 1V$ slightly decreased for fluences below 1×10^{12} p/cm^2, which was attributed to a compensation effect from iodine vacancies that shift the films from weak p-type toward an intrinsic state [131,164]. However, as fluence increased to 1×10^{14} p/cm^2, the dark current surged by nearly three orders of magnitude. Additionally, the dark I–V curves transitioned from anticlockwise to clockwise hysteresis under positive bias, suggesting that proton-induced ionic defects, especially shallow-level iodine vacancies, significantly alter carrier densities and contribute to device degradation [131,164–166]. The SRIM simulations done by Martinez et al. are in line with the above claim. Fig. 8(e) and (f) show the distribution of C, H, N, Pb, and I atom vacancies in the perovskite layer for 1 and 10 MeV proton irradiation. Notably, vacancies are predominantly observed for I and Pb ions. They also noted an increase in their density as the proton energy decreases. For instance, 1 MeV protons yield nearly 10^{-5} collisions per ion with iodide ions—a frequency that drops by almost an order of magnitude at 10 MeV. Furthermore, although hydrogen has a low atomic number, its high abundance (approximately six times that of carbon and nitrogen) in the perovskite results in a comparatively elevated collision rate, whereas carbon and nitrogen experience fewer collisions due to their lower concentrations. Thus, the interplay between displacement cascades and vacancy formation critically shapes the defect landscape in perovskites under proton irradiation [37]. These findings suggest that iodine defects dominate the defect landscape, shallow iodine vacancies drive early-stage changes in electrical behavior, and their accumulation at higher fluences leads to catastrophic increases in leakage currents.

Extending the vacancy analysis, the focus is now placed on the atom-specific contributions to vacancy formation. Fig. 8(g) and (h) shows the total damage profiles produced by various proton energies irradiating the III−V cell and PSC, respectively. In conventional semiconductor cells

such as InGaP$_2$ and GaAs, SRIM simulations indicate that LEO protons (protons with energies 0.1, 0.5, 1 and 10 MeV) induce vacancies with distributions of approximately 27 % In, 27 % Ga, and 45 % P in InGaP$_2$ and roughly 50 % Ga and 50 % As in GaAs [90]. In contrast, tin-lead perovskites predominantly exhibit iodine vacancies, which account for about 50 % of the total defects, while tin and lead each contribute less than 10 %, and hydrogen slightly more than 10 % [87]. In a study on MAPbI$_3$ by Huang et al., iodine vacancies were reported to represent approximately 55 % of the total defects. Additional simulations using protons of energy less than 1 MeV reveal that within perovskites, hydrogen and iodine atoms are the most susceptible to displacement. However, due to their low mass, displaced hydrogen atoms are likely to be healed by migrating back to their initial position. The removal of hydrogen from the organic A site, where formamidinium and methylammonium reside, leads to deprotonation and the formation of iodine interstitials [131]. These findings show strong energy-dependent behavior in vacancy formation. This defect profile, which features self-healing tendencies for hydrogen defects, contributes to the enhanced radiation hardness of PSCs when compared to conventional InGaP$_2$ and GaAs devices.

Alongside the reported atom displacement and bond breakage, other studies have focused on how irradiation leads to the formation of trap states that alter charge density, carrier lifetime, and recombination dynamics. Barbé et al. determined that irradiation at fluences of 10^{12}-10^{13} p/cm^2 leads to an increased charge density due to trap formation, which prolongs the carrier lifetime by temporarily capturing minority carriers in shallow traps. However, at 10^{14} p/cm^2, fast interfacial recombination dominates, significantly reducing the lifetime without substantially affecting the bulk recombination, indicating that performance loss is mainly due to degradation of the spiro-OMeTAD interface rather than changes in the perovskite layer [29]. It is crucial to study how light intensity-dependent J_{sc} and V_{oc} behave under the influence of proton irradiation to understand more about the recombination dynamics observed in the PSCs [89,167]. The relationship between the J_{sc} and V_{oc} with the light intensity is given in Equations (1) and (2), respectively.

$$log \ J_{sc} = \alpha \log L \tag{1}$$

$$V_{oc} \propto S \frac{KT}{q} \times \ln L \tag{2}$$

L is the light intensity, k is the Boltzmann constant, T is the absolute temperature, q is the elementary charge, α is a proportionality constant, and S is a factor that determines the dominant recombination mechanism [26,89,168]. $S = 1$ indicates band-to-band recombination, $S < 1$ indicates surface-trap assisted recombination and $S > 1$ indicates bulk-trap assisted recombination [89,169–172]. Parkhomenko et al. irradiated the device with 140 keV protons via short pulses (150ns) up to the fluence of 6×10^{12} p/cm^2. After irradiation, the value of α decreased from 0.9834 to 0.9395, indicating the increase in the band-to-band recombination due to protons. As seen in Equation (2), V_{oc} exhibits a semi-logarithmic dependence on light intensity, meaning V_{oc} is proportional to the natural logarithm of light intensity. Fig. 8(i) shows the dependence of V_{oc} on the light intensity for devices before and after irradiation. Parkhomenko et al. reported a linear relationship in the semi-logarithmic plot for the pristine devices; in contrast, the irradiated devices showed a non-linear behavior at lower light intensity, indicating a decrease in the shunt resistance (R_{sh}) [89]. This behavior was attributed to the increase in leakage currents and recombination losses [89, 173–178]. To understand more about the dominant recombination pathway, the first (k_1), second (k_2), and third (k_3) order recombination coefficients, and the changes in these values are listed in Table 3. There was a huge increase in the value of k_1 implying that the dominant recombination pathway was SRH recombination and, as evidenced in the increase in the value of k_2, band-to-band recombination also contributed to the total recombination. However, there was no

Table 3
The first, second, and third-order recombination coefficients for devices before and after irradiation as reported by Parkhomenko et al. [89].

Sample	Pristine	Irradiated
k_1 (s^{-1})	5.69	49.81
k_2 $(10^{-14}\ cm^3\ s^{-1})$	1.85	3.62
k_3 $(\times\ 10^{-11}\ s^{-1})$	1.50	1.18

significant change in the contribution from the surface trap-assisted recombination to the total recombination [89]. Consistent with this result, Lang et al. fitted the Suns-V_{oc} data and calculated the increase in the S value from 1.41 to 1.46 after irradiation with a 68 MeV proton beam and one more study reported the increase of S value from 1.19 to 2.04 [27,118]. This suggests that the contribution of the SRH recombination to the total recombination is higher than the other types of recombination [27,179,180]. According to SRH statistics, SRH recombination increases the deep traps that function as recombination centers [26,118,181].

Proton irradiation induces both structural and electronic defects in PSCs that evolve with fluence. At lower fluences, trap formation temporarily prolongs carrier lifetime, while at higher fluences, increased vacancy formation, particularly of iodine, enhances nonradiative SRH and band to band recombination. These changes reduce R_{sh} and increase leakage currents, contributing to overall performance degradation, especially through damage at the spiro-OMeTAD interface. Notably, iodine vacancies are linked to further thermal and photochemical degradation, underscoring the importance of effective halide passivation; current strategies include organic doping along grain boundaries [100].

To reduce displacement damage in PSCs, one promising strategy is to develop more robust materials. By increasing the bonding strength of halogen atoms and improving the phase stability of perovskites, the energy needed to knock atoms out of place can be increased [98]. For example, Liu et al. found that adding Mn^{2+} to $CsPbCl_3$ nanocrystals increased the lifetime under 200 keV electron radiation by ten times and increased the phase stability [98,182]. In addition, thermal treatments such as equal temperature interval and equal time interval annealing can help repair radiation damage by reducing the number of defects. These heat treatments extend the lifetime of devices by restoring performance in damaged areas, offering a practical method for in-orbit repair [98]. Passivation and iodine capture are promising strategies for enhancing the radiation resistance of PSCs in space. For instance, Huang et al. observed that exposure to oxygen in ambient air effectively passivated iodine vacancies and repaired defects in the material [131].

Having outlined the layer-specific and the device-level degradation pathways in PSCs, it is essential to consolidate these insights. Proton irradiation produces an energy- and fluence-dependent damage profile: low-energy protons drive vacancy formation through nuclear collisions, while high-energy protons trigger ionization, radiolysis, and volatile byproduct release. Iodine vacancies dominate the defect landscape, acting as deep recombination centers, while hydrogen defects partially self-heal. These processes manifest as trap-assisted carrier lifetime extension at low fluences but evolve into SRH and band-to-band recombination at higher doses, causing leakage currents, reduced shunt resistance, and hysteresis shifts. Device instability is further aggravated by ion migration, such as Au penetration into Spiro-OMeTAD and Pb diffusion into ETL, highlighting interfacial sensitivity. Mitigation strategies include compositional engineering to suppress iodine migration, defect passivation and vacancy capture, thermal annealing for defect repair, and robust encapsulation or carbon electrodes to limit electrode diffusion. Collectively, these approaches emphasize that while PSCs display greater proton tolerance than III–V counterparts, long-term stability depends on controlling vacancy formation, protecting interfaces, and integrating self-healing mechanisms.

Along with the experiments, it is equally important to recognize the limitations of simulation tools such as SRIM. The model treats the absorber as a uniform target defined only by thickness, without considering lateral dimensions (length and breadth) or microstructural complexity. Moreover, SRIM inherently neglects dynamic processes such as defect recombination, annealing, and chemical interactions, which explains the discrepancies often observed between its predictions and experimental outcomes. Nevertheless, reliable simulations remain invaluable as they allow researchers to pre-screen materials and conditions, reducing experimental costs and resources by guiding which irradiation regimes are most relevant to validate experimentally.

3.6. Self-healing of PSCs

Despite the adverse effects of proton irradiation on PSCs, several studies have reported self-healing behavior in these devices. The recovery in device performance over time following proton exposure is detailed. Various mechanisms were observed in different papers for self-healing.

Self-healing in PSCs by promoting defect reorganization through ion migration was observed post-proton irradiation. Microscopic heating provides the energy for halide interstitials to fill vacancies, effectively annealing the lattice [43]. This effect is reflected in J-V curves (Fig. 9 (a)), which shows an increase in V_{oc} after 300 keV irradiation, consistent with defect passivation and interface healing. In addition, protons may cause joule heating in the perovskite, which further assists in healing defects via thermal annealing [43,104]. Displaced ions, particularly iodide and hydrogen, remain mobile at room temperature and enhance defect recovery through interstitial-vacancy recombination as reflected in the enhanced PL intensity under 2 MeV exposure at low fluence (Fig. 9 (b)) [104,183,184]. Storage in the dark further improves performance, likely because fast ion migration heals residual lattice defects [128]. Brus et al. reported that ion migration plays a critical role in restoring an energetically favorable defect configuration and reducing nonradiative recombination losses [26]. Together, these findings indicate that the self-healing phenomenon in PSCs is primarily driven by ion migration, which reorganizes defects and enhances overall PV performance.

In addition to ion migration, the generation and compensation of shallow defect states further enhance self-healing in PSCs. Brus et al. demonstrated that the formation of these shallow states is critical for restoring device performance [26]. In $(FASn)_{0.6}(MAPb)_{0.4}I_3$, iodide displacement creates shallow defects that are inherently mobile and promote defect reorganization [87,107,185–187]. In this system, Sn^{4+} vacancies near grain boundaries and interfaces serve to passivate additional defects and reduce nonradiative losses [120]. Although proton irradiation introduces extra defects, the preexisting impurity background helps passivate them so that the impact is limited to inhibited carrier collection rather than increased SRH recombination losses [26, 27,40,87,107,120]. Moreover, high-energy proton exposure transforms deep traps into shallow states by generating Frenkel defects, imparting a positive doping effect that compensates for the enhanced recombination of deep defects. This behavior is reflected in the V_{oc}-lin(light intensity) characteristics (Fig. 9(c)), where the slope decreases from 1.40 kT in the control to 1.13 kT in irradiated devices, confirming reduced SRH recombination losses. [26,37]. Irradiation-induced point defects in the inorganic Pb–I framework further create shallow carrier traps that offset deep traps associated with organic degradation [104,188]. Finally, the soft and dynamic nature of the perovskite lattice allows these shallow defects to be unstable and to revert to near-pristine conditions over time; however, while self-recovery is readily observed at low fluences, at high proton fluences stable defect complexes form that inhibit healing and ultimately reduce performance [104,111].

While the formation and compensation of shallow traps provide a pathway for defect recovery, electronic ionization healing contributes by reconfiguring interface defects into more favorable states. Electronic ionization healing refers to the process by which increased electronic energy loss during proton irradiation supplies energy that drives the
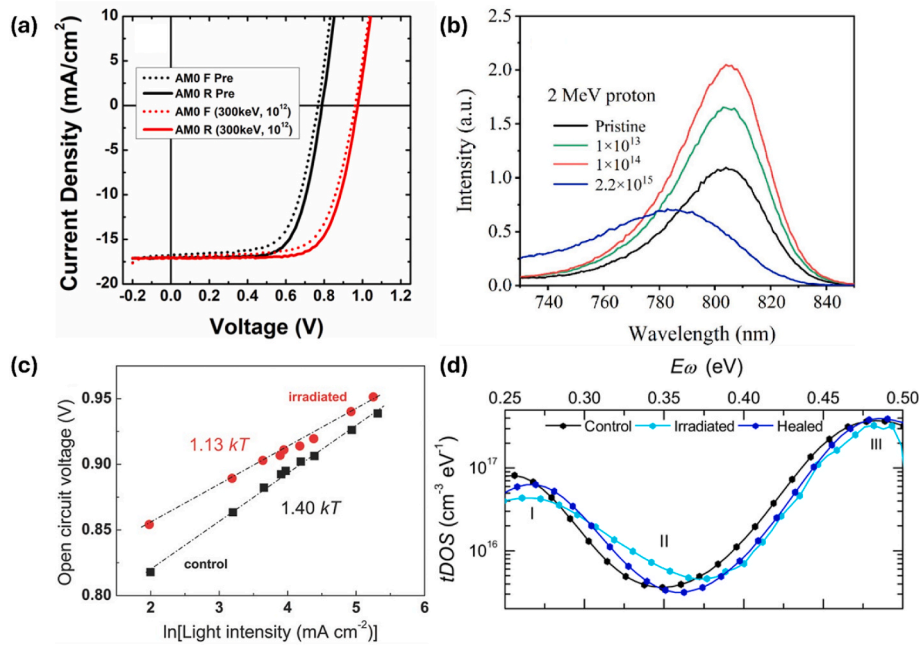
Fig. 9. (a) Current density-voltage characteristics curves under AM0 illumination before and after 300 keV proton irradiation (adapted from Ref. [43], Copyright © 2021, American Chemical Society) [43], (b) PL spectra of the perovskite films before and after 2 MeV proton irradiations (adapted with permission from Ref. [104], © 2022 Elsevier B.V.), (c) Open circuit voltage versus light intensity of the control and irradiated solar cells in the semi logarithmic scale (adapted with prmission from Ref. [26], © 2017 WILEY-VCH Verlag GmbH & Co. KGaA, Weinheim) (d) Trap density of states (tDOS) of the PSCs before irradiation (black), after irradiation with the NIEL-dominated single dose of 0.06 MeV protons (cyan), and after being healed with dual dose radiation (blue) with IEL x = 3.6 (adapted from Ref. [154], Copyright © 2024, The Author(s)). (For interpretation of the references to color in this figure legend, the reader is referred to the Web version of this article.)

reorganization of defects into more favorable configurations, thereby enhancing device performance. In PSCs, particularly at proton energies around 300 keV, this effect improves the V_{oc} by healing interface defects [43,90]. Additional mechanisms beyond those already discussed include improved interface healing via enhanced doping of the spiro-OMeTAD contact and irradiation-induced phase segregation that forms domains with higher phase purity [37,104].

Kirmani et al. demonstrated that dual-dose irradiation improves defect healing in PSCs by combining low-energy and high-energy proton exposures. Low-energy (0.06 MeV) protons generate many vacancies via significant NIEL, while 1.0 MeV protons contribute additional ionizing energy that induces local phonon vibrations, enabling displaced iodine atoms to reoccupy vacancies and reduce deep trap density. Experimentally, single-dose devices show an initial PCE remaining factor of ~0.59 versus ~0.65 for dual-dose devices; after 10 days of dark aging, both improve to ~0.77, and 60 °C annealing raises the single-dose PCE factor to ~0.85 within 5 h. Fig. 9(d) shows that there was a significant reduction in deep trap density after the dual dose treatment. Dual dose devices also exhibit higher thermal resilience at 90 °C, confirming that increased ionizing energy loss facilitates thermally activated defect recovery [154].

Although these studies suggest strong potential for proton-irradiation-induced self-healing in devices, a radiation threshold exists beyond which this healing effect is no longer observed. This makes it important to use a radiation-hard encapsulation material to protect the devices in space missions [111]. Some studies used polymer film for encapsulation and observed the formation of color centers. Cerium-doped space-grade glass can be used to encapsulate the device, as it is qualified for use in space conditions, primarily because it forms fewer color centers than cerium-free glass [133,189].

3.7. Changes in PV performance after proton irradiation

In this section, the effects of proton irradiation on PV parameters such as PCE, J_{sc}, V_{oc}, and fill factor (FF) are explained and explore the

mechanisms behind the observed degradation or self-healing behaviors. Table 4 has a comprehensive list of PCEs observed before and after proton irradiation from various studies. The fluence and energy of the proton beam varied over a large range, and the table includes various conditions such as low temperature, low light intensity, tandem solar cells, various ratios of I/Br, usage of the short-pulsed proton beam, PCE testing for different time intervals, and energy-tuned dual irradiation dosing. The table highlights that the PCE decrease is directly related to the increase in the fluence and is severely compromised at higher fluence [48].

The disruptions in the bonds cause the decline in the J_{sc}, V_{oc}, and the FF of the device [31]. The J_{sc} degradation indicates the defect generation that might cause permanent vacancies or poor crystallinity, with a modified Fermi level resulting in poor charge collection properties [37]. Increased SRH recombination due to vacancies reducing the carrier lifetime can also lead to a decrease in the J_{sc} [37,190–192]. One more reason for the J_{sc} drop is the color center formation [98]. Costa et al. irradiated their devices having different I/Br ratios with 1 MeV protons. A slight PCE increase was seen for lower fluence due to the annealing effect; at higher fluences, FF declined rapidly due to the degradation in the layers or the interface between them [118,121]. Reduced charge transport properties due to shallow traps or defect centers can also be a reason for the decrease in the J_{sc} and the PCE of the device [111]. The degradation in the V_{oc} was attributed to the recombination losses in the PSCs, and as seen in equation (2), V_{oc} is directly related to the dominant recombination processes [118,179,181].

Proton irradiation can have complex effects on PSC performance, sometimes causing degradation, while in certain conditions, leading to performance improvement. For instance, Durant et al. reported a 20 % increase in both V_{oc}, P_{max}, significantly improving the PCE at 300 keV proton irradiation. This improvement was attributed to the increase in R_{sh} due to the passivation of the current leakage pathways at the grain boundaries [26,43]. On the other hand, Huang et al. annealed the irradiated devices for 3 days in the vacuum chamber and noticed a recovery in the cell performance due to the migration of cations and

Table 4
The changes in the PCE for PSCs for various energies and fluences according to various studies. * The specific layers affected by proton irradiation are highlighted in bold within each device structure.

Energy (MeV)	Fluence (p/cm²)	Device structure	PCE (Initial) %	PCE (Final) %		Key findings	Reference
0.05	10^{13} 10^{15}	FTO/SnO$_2$/**MAPbI$_3$/spiro-OMeTAD**/Au	16.23	12.98 ~0		Partial amorphization was observed in the perovskite layer, accompanied by the decomposition of C–H, C–O, and C=C bonds in spiro-OMeTAD.	[112]
0.05	10^{12}	ITO/NiO/MAPbI$_3$/PCBM/Ag	12.3	~7.5 12.5 (After vacuum annealing)		The study does not explicitly assign the degradation to a single layer, there was a dramatic increase in series resistance (3.8–24.5 Ω·cm²).	[129]
0.05	10^{10} 10^{11} 10^{12}	ITO/PolyTPD/PFN-Br/**FA$_{0.8}$Cs$_{0.2}$PbI$_{2.4}$Br$_{0.6}$Cl$_{0.02}$**/LiF/PEIE/ SnO$_2$/ZnO/ITO/Al$_2$O$_3$	6.59 5.52 5.56	6.47 5.77 4.49		Vacancy formation led to the degradation.	[43]
0.075 (−170^0 C)	4.3×10^{13}	ITO/NiO$_x$/PTAA/**Cs$_{0.22}$FA$_{0.78}$Pb(Cl$_{0.03}$Br$_{0.15}$I$_{0.85}$)$_3$**/C$_{60}$/BCP/ SnO$_x$/IZO/Au	11.2 (19.2AU) 7.1 (5.5AU)	3.72 2.32		The perovskite layer did not degrade, the degradation is due to the CTL or CTL-perovskite interface.	[48]
0.14	6×10^{12} (3 short pulses of 150 ns)	Glass/ITO/spiro-TTB/**MAPbI$_3$**/C$_{60}$/BCP/Cu	13.43	7.14		Broken covalent bon**d**s in the perovskite structure led to the creation of defect states within the bandgap.	[89]
0.15	10^{12} 10^{15}	Quartz/AZO/SnO$_2$/Cs$_{0.05}$(MA$_{0.17}$FA$_{0.83}$)$_{0.95}$ Pb(I$_{0.83}$Br$_{0.17}$)$_3$/**spiro-OMeTAD**/Ag	15	~17 ~ 0		The degradation in spiro-OMeTAD led to a weaker charge extraction and increased interfacial recombination.	[29]
0.17	2×10^{12} 10^{13}	glass/FTO/SnO$_2$ QDs/SnO$_2$ NPs/ **Cs$_{0.04}$Rb$_{0.04}$(FA$_{0.65}$MA$_{0.35}$)$_{0.92}$Pb(I$_{0.85}$Br$_{0.14}$Cl$_{0.05}$)$_3$**/Spiro-OMeTAd/Au	18.01	14.75 7.84		Degradation was attributed to increased non-radiative recombination resulting from proton-induced deep traps in the bulk.	[118]
1	(a) 10^{13} (b) 5×10^{14}	ITO/SnO$_2$/Cs$_{0.05}$FA$_{1.95}$Pb(I$_{(1-y)}$Br$_y$)$_3$/**PTAA**/Au y = 0.09 y = 0.17 y = 0.25 y = 0.33	5.2 8.1 5.72 7.79	(a) 5.6 8.7 6.9 8.5	(b) 2.2 3.9 4.5 4.1	optical loss in PTAA and increased contact resistance were observed. Devices preserved performance when pristine PTAA was applied after perovskite irradiation.	[121]
3.7	10^{11}	ITO/PEDOT/**(FASn)$_{0.6}$(MAPb)$_{0.4}$I$_3$**/PCBM/C$_{60}$/TmPyPB/Ag	13	12.4		SRIM revealed that vacancy formation led to the degradation of the perovskite layer.	[87]
10	7.9×10^{10}	FTO/TiO$_2$/**MAPbI$_3$**/Spiro-OMeTAD/Au	7.15	6.95		Increased ion vacancies, defect states, and recombination losses.	[37]
10	10^{14}	Glass/ITO/SnO$_2$/**Cs$_{0.1}$FA$_{0.9}$PbI$_3$**/spiro-OMeTAD/Au	24.1	21.4		Void formation and surface ablation were observed in the perovskite layer.	[108]
68	1.02×10^{12}	ITO/PEDOT:PSS/**MAPbI$_3$**/PC$_{61}$BM/BCP/Ag	4.70	5.70		High-energy protons formed shallow, benign defects in the perovskite that reduced non-radiative losses and improved device performance.	[26]
68	10^{12}	Quartz/ITO/PTAA/**Cs$_{0.05}$(MA$_{0.17}$FA$_{0.83}$)$_{0.95}$ Pb(I$_{0.83}$Br$_{0.17}$)$_3$**/C$_{60}$/BCP/Cu	18.8	17.8		Proton-induced traps were formed due to Iodine interstitials and vacancies in the perovskite layer.	[27]
68	2×10^{12}	LiF/IZO/SnO$_2$/C$_{60}$/Cs$_{0.05}$(MA$_{0.17}$FA$_{0.83}$)$_{0.95}$Pb(I$_{0.83}$Br$_{0.17}$)$_3$/ PTAA/**NiO$_x$**/ZnO/CdS/**CIGS**/Mo/glass	15.2	12.6		The perovskite layer was intact in both the tandem solar cells.	[40]
		LiF/IZO/SnO$_2$/C$_{60}$/Pvsk/PTAA/ITO/ncSiO$_x$/**(i)-a-Si:H/(n)-C-Si/(i)-a-Si:H/(p)-a-Si:H**/Al:ZnO/Ag	18.8	0.16			
0.06 0.06 + 1 1	10^{13} $10^{13}+10^{14}$ 3.8×10^{14}	Quartz/ITO/SnO$_2$/**Cs$_{0.05}$(FA$_{0.83}$MA$_{0.17}$)$_{0.95}$Pb(I$_{0.83}$Br$_{0.17}$)$_3$**/ **spiro-OMeTAD**/Au	16 16.29 17.63	12.16 12.25 11.57		The perovskite layer was the major damage source, and spiro-OMeTAD made a minor contribution.	[154]
0.06 0.06 + 1 1	10^{13} $10^{13}+10^{14}$ 3.8×10^{14}	Quartz/ITO/PTAA/**Cs$_{0.05}$(FA$_{0.83}$ MA$_{0.17}$)$_{0.95}$Pb(I$_{0.83}$Br$_{0.17}$)$_3$**/ C$_{60}$/BCP/Ag	18.72 18.5 17.54	13.5 8.12 4.77		The perovskite layer is the only identified source of degradation, and it is fully or partially healed by IEL-induced annealing.	[154]
0.075 0.3 1	10^{13} 10^{14} 4×10^{14}	ITO/PolyTPD/PFN-Br/**FA$_{0.8}$Cs$_{0.2}$PbI$_{2.4}$Br$_{0.6}$Cl$_{0.02}$**/LIF/C$_{60}$/ SnO$_2$/ITO/Al$_2$O	11	0days 10.67 10.56 6.93	2 months 9.02 7.59 –	SRIM simulations show uniform vacancy formation across the entire perovskite layer. This paper does not describe the resistance of HTL and ETL.	[111]

anions to their original position [129].

4. Conclusion

In conclusion, this review comprehensively showed how proton irradiation affects the PSCs, tracing its influence from the fundamental interaction mechanisms to material- and device-level consequences. Proton interaction in PSCs involves both nuclear and electronic effects, with SRIM simulations confirming that nuclear collisions dominate at low energies, leading to displacement of atoms and formation of defects within the perovskite lattice. These defects, particularly vacancies and interstitials, act as carrier traps and contribute to degradation of photovoltaic parameters. At higher proton energies, energy loss occurs predominantly through electronic ionization, which, although less damaging structurally, still affects device performance.

The effects of proton irradiation were further explored in relation to perovskite films and full PSC architecture. Studies show that radiation damage is not uniformly distributed across the device. Within the substrate category, flexible substrates like PET and PEN offer advantages in terms of mass and mechanical resilience but show greater vulnerability to radiation-induced degradation compared to rigid substrates. Rigid materials such as fused silica and cerium-doped glass demonstrated superior resistance to optical and structural damage, making them more suitable for space environments.

TCOs also show varied responses. FTO degrades under high fluence, with increased resistivity and reduced transmittance, while ITO demonstrates excellent stability in both electrical and optical properties, making it more suitable for space environments. AZO and IZO exhibited mixed behavior, with changes dependent on fluence and proton energy. For top electrodes, silver and gold experienced degradation in conductivity and surface morphology, while carbon-based electrodes, especially in mesoporous configurations, exhibited exceptional resilience, owing to their thickness and ability to absorb incoming protons.

CTLs play a critical role in determining the radiation resilience of PSCs. Metal oxide ETLs such as SnO_2 and TiO_2 show strong tolerance to proton irradiation, while metal oxide HTLs like NiO_x have shown promising stability in device-level tests, though their isolated behavior remains unclear. Organic HTLs like spiro-OMeTAD are highly susceptible to damage, whereas organic ETLs such as PCBM demonstrate moderate stability, particularly when blended with robust donor polymers. CTL-free architecture presents a potential solution, but its radiation response remains largely untested.

Self-healing behavior post-irradiation was also reported in certain studies, attributed to ion migration, defect passivation, interfacial doping, and phase segregation. However, this effect was limited to moderate fluences, beyond which irreversible degradation occurred. Despite these limitations, PSCs showed better radiation tolerance compared to conventional photovoltaic technologies such as silicon, CIGS, and multi-junction cells.

Overall, understanding the material-specific and layer-dependent responses to proton irradiation provides a foundation for engineering more resilient PSCs. By optimizing halide composition, implementing robust CTL-free designs, and incorporating radiation-tolerant TCOs and encapsulation strategies, PSCs can be further developed as reliable power sources for future space missions. Although substantial evidence supports proton-induced changes in the devices, the underlying mechanisms responsible for these effects remain to be fully understood.

CRediT authorship contribution statement

Harini Srikanth Rao: Writing – original draft. **Wei-Hao Chiu:** Formal analysis, Data curation. **Shih-Hsuan Chen:** Formal analysis. **Ming-Chung Wu:** Writing – review & editing, Conceptualization. **Kun-Mu Lee:** Writing – review & editing, Conceptualization.

Declaration of generative AI and AI-assisted technologies in the writing process

During the preparation of this work, the authors used ChatGPT (free version based on GPT-3.5, developed by OpenAI) to improve the readability of the review. The AI tool was not used to generate any images or to analyze data. After using this tool, the authors reviewed and edited the content as needed and take full responsibility for the content of the published article.

Declaration of competing interest

The authors declare that they have no known competing financial interests or personal relationships that could have appeared to influence the work reported in this paper.

Acknowledgement

Appendix A. Supplementary data

Supplementary data to this article can be found online at https://doi.org/10.1016/j.solmat.2025.114015.

Data availability

Data will be made available on request.

References

[1] NASA, Clarreo. https://science.nasa.gov/mission/clarreo-pathfinder/, 2023.
[2] NASA, DAVINCI. https://science.nasa.gov/mission/davinci/, 2025.
[3] NASA, Asthros. https://science.nasa.gov/mission/asthros/, 2024.
[4] NASA, Dragonfly. https://science.nasa.gov/mission/dragonfly/, 2024.
[5] J. Li, A. Aierken, Y. Liu, Y. Zhuang, X. Yang, J. Mo, R. Fan, Q. Chen, S. Zhang, Y. Huang, A brief review of high efficiency III-V solar cells for space application, Front. Physiol. 8 (2021) 631925, https://doi.org/10.3389/fphy.2020.631925.
[6] D.J. Flood, Space photovoltaics–history, progress and promise, Mod. Phys. Lett. B 15 (2001) 561–570, https://doi.org/10.1142/S0217984901002038.
[7] R. Pandey, R. Chaujar, Technology computer aided design of 29.5% efficient perovskite/interdigitated back contact silicon heterojunction mechanically stacked tandem solar cell for energy-efficient applications, J. Photon. Energy 7 (2017), https://doi.org/10.1117/1.JPE.7.022503, 022503-022503.
[8] R. Pandey, A. Singla, J. Madan, R. Sharma, R. Chaujar, Toward the design of monolithic 23.1% efficient hysteresis and moisture free perovskite/c-Si HJ tandem solar cell: a numerical simulation study, J. Micromech. Microeng. 29 (2019) 064001, https://doi.org/10.1088/1361-6439/ab1512.
[9] R. Pandey, A. Khanna, K. Singh, S.K. Patel, H. Singh, J. Madan, Device simulations: toward the design of> 13% efficient PbS colloidal quantum dot solar cell, Sol. Energy 207 (2020) 893–902, https://doi.org/10.1016/j.solener.2020.06.099.
[10] N. Zarrabi, O.J. Sandberg, S. Zeiske, W. Li, D.B. Riley, P. Meredith, A. Armin, Charge-generating mid-gap trap states define the thermodynamic limit of organic photovoltaic devices, Nat. Commun. 11 (2020) 5567, https://doi.org/10.1038/s41467-020-19434-0.
[11] L. Zhan, S. Li, T.-K. Lau, Y. Cui, X. Lu, M. Shi, C.-Z. Li, H. Li, J. Hou, H. Chen, Over 17% efficiency ternary organic solar cells enabled by two non-fullerene acceptors working in an alloy-like model, Energy Environ. Sci. 13 (2020) 635–645, https://doi.org/10.1039/C9EE03710A.
[12] J. Li, J. Duan, X. Yang, Y. Duan, P. Yang, Q. Tang, Review on recent progress of lead-free halide perovskites in optoelectronic applications, Nano Energy 80 (2021) 105526, https://doi.org/10.1016/j.nanoen.2020.105526.
[13] J. Yu, J. Li, Y. Zhao, A. Lambertz, T. Chen, W. Duan, W. Liu, X. Yang, Y. Huang, K. Ding, Copper metallization of electrodes for silicon heterojunction solar cells: process, reliability and challenges, Sol. Energy Mater. Sol. Cells 224 (2021) 110993, https://doi.org/10.1016/j.solmat.2021.110993.
[14] R. Pandey, R. Chaujar, Numerical simulation of rear contact silicon solar cell with a novel front surface design for the suppression of interface recombination and improved absorption, Curr, Appl. Phys. 16 (2016) 1581–1587, https://doi.org/10.1016/j.cap.2016.09.002.

[15] R. Pandey, R. Chaujar, Numerical simulations: toward the design of 27.6% efficient four-terminal semi-transparent perovskite/SiC passivated rear contact silicon tandem solar cell, Superlattice. Microst. 100 (2016) 656–666, https://doi.org/10.1016/j.spmi.2016.10.033.

[16] R. Pandey, R. Chaujar, Rear contact silicon solar cells with a-SiCX: h based front surface passivation for near-ultraviolet radiation stability, Superlattice. Microst. 122 (2018) 111–123, https://doi.org/10.1016/j.spmi.2018.08.016.

[17] L. Oberbeck, K. Alvino, B. Goraya, M. Jubault, IPVF's PV technology vision for 2030, Prog. Photovoltaics Res. Appl. 28 (2020) 1207–1214, https://doi.org/10.1002/pip.3305.

[18] P. Roy, N.K. Sinha, S. Tiwari, A. Khare, A review on perovskite solar cells: evolution of architecture, fabrication techniques, commercialization issues and status, Sol. Energy 198 (2020) 665–688, https://doi.org/10.1016/j.solener.2020.01.080.

[19] H. Chen, C. Liu, J. Xu, A. Maxwell, W. Zhou, Y. Yang, Q. Zhou, A.S. Bati, H. Wan, Z. Wang, Improved charge extraction in inverted perovskite solar cells with dual-site-binding ligands, Science 384 (2024) 189–193, https://doi.org/10.1126/science.adm9474.

[20] A. Kojima, K. Teshima, Y. Shirai, T. Miyasaka, Organometal halide perovskites as visible-light sensitizers for photovoltaic cells, J. Am. Chem. Soc. 131 (2009) 6050–6051, https://doi.org/10.1021/ja809598r.

[21] W. Shockley, H. Queisser, Detailed balance limit of efficiency of p–n junction solar cells, in: Renewable Energy, Routledge, 2018. Vol2_35-Vol32_54.

[22] National Renewable Energy Laboratory (NREL), Best research-cell efficiency chart. https://www.nrel.gov/pv/cell-efficiency, 2025.

[23] N.K. Tailor, M. Abdi-Jalebi, V. Gupta, H. Hu, M.I. Dar, G. Li, S. Satapathi, Recent progress in morphology optimization in perovskite solar cell, J. Mater. Chem. A 8 (2020) 21356–21386, https://doi.org/10.1039/D0TA00143K.

[24] M. Kaltenbrunner, G. Adam, E.D. Głowacki, M. Drack, R. Schwödiauer, L. Leonat, D.H. Apaydin, H. Groiss, M.C. Scharber, M.S. White, Flexible high power-per-weight perovskite solar cells with chromium oxide–metal contacts for improved stability in air, Nat. Mater. 14 (2015) 1032–1039, https://doi.org/10.1038/nmat4388.

[25] S. Tao, I. Schmidt, G. Brocks, J. Jiang, I. Tranca, K. Meerholz, S. Olthof, Absolute energy level positions in tin-and lead-based halide perovskites, Nat. Commun. 10 (2019) 2560, https://doi.org/10.1038/s41467-019-10468-7.

[26] V.V. Brus, F. Lang, J. Bundesmann, S. Seidel, A. Denker, B. Rech, G. Landi, H.C. Neitzert, J. Rappich, N.H. Nickel, Defect dynamics in proton irradiated CH3NH3PbI3 perovskite solar cells, Adv. Electron. Mater. 3 (2017) 1600438, https://doi.org/10.1002/aelm.201600438.

[27] F. Lang, M. Jošt, J. Bundesmann, A. Denker, S. Albrecht, G. Landi, H.-C. Neitzert, J. Rappich, N.H. Nickel, Efficient minority carrier detrapping mediating the radiation hardness of triple-cation perovskite solar cells under proton irradiation, Energy Environ. Sci. 12 (2019) 1634–1647, https://doi.org/10.1039/C9EE00077A.

[28] C. Tao, S. Neutzner, L. Colella, S. Marras, A.R.S. Kandada, M. Gandini, M. De Bastiani, G. Pace, L. Manna, M. Caironi, 17.6% stabilized efficiency in low-temperature processed planar perovskite solar cells, Energy Environ. Sci. 8 (2015) 2365–2370, https://doi.org/10.1039/C5EE01720C.

[29] J. Barbé, D. Hughes, Z. Wei, A. Pockett, H.K. Lee, K.C. Heasman, M.J. Carnie, T.M. Watson, W.C. Tsoi, Radiation hardness of perovskite solar cells based on Aluminum-Doped zinc oxide electrode under Proton irradiation, Sol. RRL 3 (2019) 1900219, https://doi.org/10.1002/solr.201900219.

[30] A.W. Ho-Baillie, H.G. Sullivan, T.A. Bannerman, H.P. Talathi, J. Bing, S. Tang, A. Xu, D. Bhattacharyya, I.H. Cairns, D.R. McKenzie, Deployment opportunities for space photovoltaics and the prospects for perovskite solar cells, Adv. Mater. Technol. 7 (2022) 2101059, https://doi.org/10.1002/admt.202101059.

[31] O. Malinkiewicz, M. Imaizumi, S.B. Sapkota, T. Ohshima, S. Öz, Radiation effects on the performance of flexible perovskite solar cells for space applications, Emergent Mater 3 (2020) 9–14, https://doi.org/10.1007/s42247-020-00071-8.

[32] A.R. Kirmani, B.K. Durant, J. Grandidier, N.M. Haegel, M.D. Kelzenberg, Y. M. Lao, M.D. McGehee, L. McMillon-Brown, D.P. Ostrowski, T.J. Peshek, Countdown to perovskite space launch: guidelines to performing relevant radiation-hardness experiments, Joule 6 (2022) 1015–1031, https://doi.org/10.1016/j.joule.2022.03.004.

[33] B.A. Seid, S. Sarisozen, F. Peña-Camargo, S. Ozen, E. Gutierrez-Partida, E. Solano, J.A. Steele, M. Stolterfoht, D. Neher, F. Lang, Understanding and mitigating atomic oxygen-induced degradation of perovskite solar cells for near-earth space applications, Small (2024) 2311097, https://doi.org/10.1002/smll.202311097.

[34] B. Mukherjee, X. Wu, T. Maczka, T. Kwan, Y. Huang, V. Mares, Near space radiation dosimetry in Australian outback using a balloon borne energy compensated PIN diode detector, Radiat. Meas. 94 (2016) 65–72, https://doi.org/10.1016/j.radmeas.2016.09.007.

[35] D. Yu, P. Wang, F. Cao, Y. Gu, J. Liu, Z. Han, B. Huang, Y. Zou, X. Xu, H. Zeng, Two-dimensional halide perovskite as β-ray scintillator for nuclear radiation monitoring, Nat. Commun. 11 (2020) 3395, https://doi.org/10.1038/s41467-020-17114-7.

[36] J.I. Kleiman, M. Tagawa, Y. Kimoto, Protection of Materials and Structures from the Space Environment, Springer, 2006.

[37] W.O.H. Martínez, N.B.C. Guerrero, V.A.G. Andrade, M. Alurralde, M.D. Perez, Evaluation of the resistance of halide perovskite solar cells to high energy proton irradiation for space applications, Sol. Energy Mater. Sol. Cells 238 (2022) 111644, https://doi.org/10.1016/j.solmat.2022.111644.

[38] J.J. Loferski, The effects of electron and proton irradiation on thin film solar cells, Rev. Phys. Appl. 1 (1966) 221–227, https://doi.org/10.1051/rphysap:0196600103022101.

[39] F. Lang, G.E. Eperon, K. Frohna, E.M. Tennyson, A. Al-Ashouri, G. Kourkafas, J. Bundesmann, A. Denker, K.G. West, L.C. Hirst, Proton-radiation tolerant all-perovskite multijunction solar cells, Adv. Energy Mater. 11 (2021) 2102246, https://doi.org/10.1002/aenm.202102246.

[40] F. Lang, M. Jošt, K. Frohna, E. Köhnen, A. Al-Ashouri, A.R. Bowman, T. Bertram, A.B. Morales-Vilches, D. Koushik, E.M. Tennyson, Proton radiation hardness of perovskite tandem photovoltaics, Joule 4 (2020) 1054–1069, https://doi.org/10.1016/j.joule.2020.03.006.

[41] D.A. Lamb, C.I. Underwood, V. Barrioz, R. Gwilliam, J. Hall, M.A. Baker, S. J. Irvine, Proton irradiation of CdTe thin film photovoltaics deposited on cerium-doped space glass, Prog. Photovoltaics Res. Appl. 25 (2017) 1059–1067, https://doi.org/10.1002/pip.2923.

[42] W. Laiadi, A. Meftah, N. Sengouga, A. Meftah, Irradiation effect on the electrical characteristics of an AlGaAs/GaAs based solar cell: Comparison between electron and proton irradiation by numerical simulation, Superlattice. Microst. 58 (2013) 44–52, https://doi.org/10.1016/j.spmi.2013.03.005.

[43] B.K. Durant, H. Afshari, S. Singh, B. Rout, G.E. Eperon, I.R. Sellers, Tolerance of perovskite solar cells to targeted proton irradiation and electronic ionization induced healing, ACS Energy Lett. 6 (2021) 2362–2368, https://doi.org/10.1021/acsenergylett.1c00756.

[44] C. Leroy, P.-G. Rancoita, Principles of Radiation Interaction in Matter and Detection, World Scientific, 2011.

[45] J.F. Ziegler, M.D. Ziegler, J.P. Biersack, SRIM–The stopping and range of ions in matter (2010), Nucl. Instrum. Methods Phys. Res., Sect. B 268 (2010) 1818–1823, https://doi.org/10.1016/j.nimb.2010.02.091.

[46] W. Xiao, J. Yang, S. Xiong, D. Li, Y. Li, J. Tang, C. Duan, Q. Bao, Exploring red, green, and Blue light-activated degradation of Perovskite films and solar cells for near space applications, Sol. RRL 4 (2020) 1900394, https://doi.org/10.1002/solr.201900394.

[47] C. Barone, F. Lang, C. Mauro, G. Landi, J. Rappich, N. Nickel, B. Rech, S. Pagano, H. Neitzert, Unravelling the low-temperature metastable state in perovskite solar cells by noise spectroscopy, Sci. Rep. 6 (2016) 34675, https://doi.org/10.1038/srep34675.

[48] T. Colenbrander, J. Peng, Y. Wu, M. Kelzenberg, J.-S. Huang, C. MacFarland, D. Thorbourn, R. Kowalczyk, W. Kim, J. Brophy, Low-intensity low-temperature analysis of perovskite solar cells for deep space applications, Energy Adv 2 (2023) 298–307, https://doi.org/10.1039/D2YA00218C.

[49] G. Horneck, Space Vacuum Effects, 2015.

[50] C.A. Gueymard, D. Myers, K. Emery, Proposed reference irradiance spectra for solar energy systems testing, Sol. Energy 73 (2002) 443–467, https://doi.org/10.1016/S0038-092X(03)00005-7.

[51] A. Farooq, I.M. Hossain, S. Moghadamzadeh, J.A. Schwenzer, T. Abzieher, B. S. Richards, E. Klampaftis, U.W. Paetzold, Spectral dependence of degradation under ultraviolet light in perovskite solar cells, ACS Appl. Mater. Interfaces 10 (2018) 21985–21990, https://doi.org/10.1021/acsami.8b03024.

[52] W. Mahmoud, D. Elfiky, S. Robaa, M. Elnawawy, S. Yousef, Effect of atomic oxygen on LEO CubeSat, Int. J. Aeronaut. Space Sci. 22 (2021) 726–733, https://doi.org/10.1007/s42405-020-00336-w.

[53] R. Sun, Y. Zhang, H. Gu, X. Wang, M. Zhang, H. Li, J. Ma, L. Song, Property of protection against simultaneous action between atomic oxygen erosion and ultraviolet irradiation by MIL-53 (Al) coating, ACS Omega 9 (2024) 47324–47331, https://doi.org/10.1021/acsomega.4c08600.

[54] A. Luque, S. Hegedus, Handbook of Photovoltaic Science and Engineering, John Wiley & Sons, 2011.

[55] V. Pesce, A. Colagrossi, S. Silvestrini, Modern Spacecraft Guidance, Navigation, and Control: from System Modeling to AI and Innovative Applications, Elsevier, 2022.

[56] K.K. Degroh, B.A. Banks, D.C. Smith, Environmental durability issues for solar power systems in low Earth orbit, in: 1995 International Solar Energy Conference, 1994.

[57] P. Gordo, T. Frederico, R. Melício, S. Duzellier, A. Amorim, System for space materials evaluation in LEO environment, Adv. Space Res. 66 (2020) 307–320, https://doi.org/10.1016/j.asr.2020.03.024.

[58] T.J. Jacobsson, W. Tress, J.-P. Correa-Baena, T. Edvinsson, A. Hagfeldt, Room temperature as a goldilocks environment for CH3NH3PbI3 perovskite solar cells: the importance of temperature on device performance, J. Phys. Chem. C 120 (2016) 11382–11393, https://doi.org/10.1021/acs.jpcc.6b02858.

[59] D.J. Thomson, The seasons, global temperature, and precession, Science 268 (1995) 59–68, https://doi.org/10.1126/science.268.5207.59.

[60] NASA, Earth fact sheet. https://nssdc.gsfc.nasa.gov/planetary/factsheet/earthfact.html, 2024.

[61] L. McMillon-Brown, J.M. Luther, T.J. Peshek, What would it Take to Manufacture Perovskite Solar Cells in Space? ACS Publications, 2022 https://doi.org/10.1021/acsenergylett.2c00276.

[62] E. Grossman, I. Gouzman, Space environment effects on polymers in low earth orbit, Nucl. Instrum. Methods Phys. Res., Sect. B 208 (2003) 48–57, https://doi.org/10.1016/S0168-583X(03)00640-2.

[63] J. Plante, B. Lee, Environmental Conditions for Space Flight Hardware: a Survey, 2005.

[64] D. Jovel, M.L. Walker, Current pathways model for Hall Thruster plumes in Ground-based Vacuum Test facilities, in: AIAA Scitech 2024 Forum, 2024, p. 2365, https://doi.org/10.2514/6.2024-2365.

[65] NASA, Moon fact sheet. https://nssdc.gsfc.nasa.gov/planetary/factsheet/moonfact.html, 2024.

[66] NASA, Mars fact sheet. https://nssdc.gsfc.nasa.gov/planetary/factsheet/marsfact.html, 2024.

[67] Space, What is the temperature of Jupiter?. https://www.space.com/18391-jupiter-temperature.html, 2012.

[68] NASA, Jupiter fact sheet. https://nssdc.gsfc.nasa.gov/planetary/factsheet/jupiterfact.html, 2024.

[69] Space, Saturn's temperature: one cool planet. https://www.space.com/18473-saturn-temperature.html, 2012.

[70] NASA, Saturn fact sheet. https://nssdc.gsfc.nasa.gov/planetary/factsheet/saturnfact.html, 2025.

[71] NASA, Earth's magnetosphere and plasmasheet. https://blogs.nasa.gov/sunspot/2023/09/26/earths-magnetosphere-and-plasmasheet/, 2023.

[72] J.N. Pelton, F. Allahdadi, Handbook of Cosmic Hazards and Planetary Defense, 2015.

[73] W. Li, M. Hudson, Earth's Van Allen radiation belts: from discovery to the Van Allen Probes era, J. Geophys. Res. Space Phys. 124 (2019) 8319–8351, https://doi.org/10.1029/2018JA025940.

[74] Space Foundation, The space briefing book: types of orbits. https://www.spacefoundation.org/space_brief/types-of-orbits/.

[75] S. Vishwakarma, A.S. Chauhan, S. Aasma, A comparative Study of satellite orbits as low earth orbit (LEO) and geostationary earth orbit (GEO), SAMRIDDHI: a journal of physical sciences, Eng. Technol. 6 (2014) 99–106, https://doi.org/10.18090/samriddhi.v6i2.1559.

[76] L. Miroshnichenko, Radiation Hazard in Space, Springer Science & Business Media, 2003.

[77] P. Lantos, The Sun, the Solar Wind and Their Effects on the Earth's Environment, 2004.

[78] S. Bourdarie, M. Xapsos, The near-earth space radiation environment, IEEE Trans. Nucl. Sci. 55 (2008) 1810–1832, https://doi.org/10.1109/TNS.2008.2001409.

[79] W. Feldman, J. Asbridge, S. Bame, J. Gosling, High-speed solar wind flow parameters at 1 AU, J. Geophys. Res. 81 (1976) 5054–5060, https://doi.org/10.1029/JA081i028p05054.

[80] A.G. Boldyreva, A.F. Akbulatov, S.A. Tsarev, S.Y. Luchkin, I.S. Zhidkov, E.Z. Kurmaev, K.J. Stevenson, V.G. Petrov, P.A. Troshin, γ-ray-induced degradation in the triple-cation perovskite solar cells, J. Phys. Chem. Lett. 10 (2019) 813–818, https://doi.org/10.1021/acs.jpclett.8b03222.

[81] M. Naito, H. Kusano, S. Kodaira, Global dose distributions of neutrons and gamma-rays on the moon, Sci. Rep. 13 (2023) 13275, https://doi.org/10.1038/s41598-023-40405-0.

[82] K. Yang, K. Huang, X. Li, S. Zheng, P. Hou, J. Wang, H. Guo, H. Song, B. Li, H. Li, Radiation tolerance of perovskite solar cells under gamma ray, Org. Electron. 71 (2019) 79–84, https://doi.org/10.1016/j.orgel.2019.05.008.

[83] F. De Rossi, B. Taheri, M. Bonomo, V. Gupta, G. Renno, N.Y. Nia, P. Rech, C. Frost, C. Cazzaniga, P. Quagliotto, Neutron irradiated perovskite films and solar cells on PET substrates, Nano Energy 93 (2022) 106879, https://doi.org/10.1016/j.nanoen.2021.106879.

[84] N.P. Meredith, R.B. Horne, I. Sandberg, C. Papadimitriou, H.D. Evans, Extreme relativistic electron fluxes in the Earth's outer radiation belt: analysis of INTEGRAL IREM data, SpWea 15 (2017) 917–933, https://doi.org/10.1002/2017SW001651.

[85] Z. Song, C. Li, C. Chen, J. McNatt, W. Yoon, D. Scheiman, P.P. Jenkins, R.J. Ellingson, M.J. Heben, Y. Yan, High remaining factors in the photovoltaic performance of perovskite solar cells after high-fluence electron beam irradiations, J. Phys. Chem. C 124 (2019) 1330–1336, https://doi.org/10.1021/acs.jpcc.9b11483.

[86] D. Heynderickx, SPENVIS Space Environment Information System, 1999.

[87] B.K. Durant, H. Afshari, S. Sourabh, V. Yeddu, M.T. Bamidele, S. Singh, B. Rout, G.E. Eperon, I.R. Sellers, Radiation stability of mixed tin–lead halide perovskites: implications for space applications, Sol. Energy Mater. Sol. Cells 230 (2021) 111232, https://doi.org/10.1016/j.solmat.2021.111232.

[88] Y.C. Tan, R. Chandrasekara, C. Cheng, A. Ling, Silicon avalanche photodiode operation and lifetime analysis for small satellites, Opt. Express 21 (2013) 16946–16954, https://doi.org/10.1364/OE.21.016946.

[89] H.P. Parkhomenko, A.I. Mostovyi, M. Kaikanov, J. Strey, M.C. Turcu, M. Diederich, S.J. Wolter, V. Steckenreiter, J. Vollbrecht, V.V. Brus, Characterization of fully-evaporated perovskite solar cells and photodetectors under high-intensity pulsed proton irradiation, Sci. Rep. 14 (2024) 16735, https://doi.org/10.1038/s41598-024-67541-5.

[90] T.B. Kum, A.R. Kirmani, Critical role of low-energy protons in radiation testing of perovskite space solar cells, ACS Photonics 12 (2024) 439–446, https://doi.org/10.1021/acsphotonics.4c01818.

[91] A.I.o.A.a.A. (AIAA), AIAA S-111A-Qualification and Quality Requirements for Space Solar Cells, American Institute of Aeronautics and Astronautics, Alexander Bell Drive, Reston, VA, USA 2014 20191.

[92] E.C.f.S.S. (ECSS), ECSS-E-ST-20-08C Rev.2 – space engineering, Photovoltaic assemblies and components, ESA Requirements and Standards,Noordwijk, The Netherlands (2023).

[93] T.A. Schneider, J.A. Vaughn, K.H. Wright, B.S. Phillips, Space environment testing of photovoltaic array systems at NASA's Marshall space flight Center, in: 2015 IEEE 42nd Photovoltaic Specialist Conference (PVSC), IEEE, 2015, pp. 1–6, https://doi.org/10.1109/PVSC.2015.7355861.

[94] K. Nordlund, S.J. Zinkle, A.E. Sand, F. Granberg, R.S. Averback, R. Stoller, T. Suzudo, L. Malerba, F. Banhart, W.J. Weber, Improving atomic displacement and replacement calculations with physically realistic damage models, Nat. Commun. 9 (2018) 1084, https://doi.org/10.1038/s41467-018-03415-5.

[95] C. Marshall, R. Ladbury, P. Marshall, R. Reed, C. Howe, B. Weller, M. Mendenhall, A. Waczynski, T. Jordan, B. Fodness, Comparison of measured leakage current distributions with calculated damage energy distributions in HgCdTe, in: Radiation and its Effects on Components and Systems (RADECS) Workshop, 2006.

[96] I. Jun, W. Kim, R. Evans, Electron nonionizing energy loss for device applications, IEEE Trans. Nucl. Sci. 56 (2009) 3229–3235, https://doi.org/10.1109/TNS.2009.2033692.

[97] T. Goorley, M. James, T. Booth, F. Brown, J. Bull, L. Cox, J. Durkee, J. Elson, M. Fensin, R. Forster, Features of MCNP6, in: SNA+ MC 2013-joint International Conference on Supercomputing in Nuclear Applications+ Monte Carlo, EDP Sciences, 2014 06011, https://doi.org/10.1051/snamc/201406011.

[98] Z. Huan, Y. Zheng, K. Wang, Z. Shen, W. Ni, J. Zu, Y. Shao, Advancements in radiation resistance and reinforcement strategies of perovskite solar cells in space applications, J. Mater. Chem. A 12 (2024) 1910–1922, https://doi.org/10.1039/D3TA06388G.

[99] D. Griscom, E. Friebele, Effects of ionizing radiation on amorphous insulators, Radiat. Eff. 65 (1982) 63–72, https://doi.org/10.1080/00337578208216818.

[100] A.V. Rasmetyeva, S.S. Zyryanov, I.E. Novoselov, A.I. Kukharenko, E.V. Makarov, S.O. Cholakh, E.Z. Kurmaev, I.S. Zhidkov, Proton irradiation on halide perovskites: numerical calculations, Nanomaterials 14 (2023) 1, https://doi.org/10.3390/nano14010001.

[101] Y. Miyazawa, M. Ikegami, T. Miyasaka, T. Ohshima, M. Imaizumi, K. Hirose, Evaluation of radiation tolerance of perovskite solar cell for use in space, in: 2015 IEEE 42nd Photovoltaic Specialist Conference (PVSC), IEEE, 2015, pp. 1–4, https://doi.org/10.1109/PVSC.2015.7355859.

[102] R.A. Knief, Nuclear Energy Technology: Theory and Practice of Commercial Nuclear Power, United States, 1981.

[103] F. Bebensee, J. Zhu, J.H. Baricuatro, J.A. Farmer, Y. Bai, H.-P. Steinrück, C.T. Campbell, J.M. Gottfried, Interface formation between calcium and electron-irradiated poly (3-hexylthiophene), Langmuir 26 (2010) 9632–9639, https://doi.org/10.1021/la100209v.

[104] B. Xue, L. Zhang, Z. Li, W. Jiang, Y. Liang, N. Liu, C. Pan, L. Chen, T. Wang, Property degradation of mixed-cation perovskite films and solar cells irradiated with protons, Nucl. Instrum. Methods Phys. Res., Sect. B 526 (2022) 29–35, https://doi.org/10.1016/j.nimb.2022.06.012.

[105] M. Bartusiak, J. Becher, Proton-induced coloring of multicomponent glasses, Appl. Opt. 18 (1979) 3342–3346, https://doi.org/10.1364/AO.18.003342.

[106] A.I. Gusarov, D. Doyle, A. Hermanne, F. Berghmans, M. Fruit, G. Ulbrich, M. Blondel, Refractive-index changes caused by proton radiation in silicate optical glasses, Appl. Opt. 41 (2002) 678–684, https://doi.org/10.1364/AO.41.000678.

[107] F. Lang, N.H. Nickel, J. Bundesmann, S. Seidel, A. Denker, S. Albrecht, V.V. Brus, J. Rappich, B. Rech, G. Landi, Radiation hardness and self-healing of perovskite solar cells, Adv. Mater. 28 (2016) 8726–8731, https://doi.org/10.1002/adma.201603326.

[108] D.T. Nguyen, A.D. Bui, K. Huang, T.L. Leung, L.C. Chang, K. Nguyen, G.D. Tabi, T. Trần-Phú, H. Nguyen, A. Ho-Baillie, Void formation and radiation-induced ion migration in perovskite solar cells under 10 MeV proton radiation, Sol. RRL 8 (2024) 2400113, https://doi.org/10.1002/solr.202400113.

[109] S. Nambiar, J.T. Yeow, Polymer-composite materials for radiation protection, ACS Appl. Mater. Interfaces 4 (2012) 5717–5726, https://doi.org/10.1021/am300783d.

[110] B. Thomadsen, R. Nath, F.B. Bateman, J. Farr, C. Glisson, M.K. Islam, T. LaFrance, M.E. Moore, X.G. Xu, M. Yudelev, Potential hazard due to induced radioactivity secondary to radiotherapy: the report of task group 136 of the American association of physicists in medicine, Health Phys. 107 (2014) 442–460, https://doi.org/10.1097/HP.0000000000000139.

[111] H. Afshari, S.A. Chacon, S. Sourabh, V.R. Whiteside, R. Crawford, B. Rout, G.E. Eperon, I.R. Sellers, Radiation tolerance and self-healing in triple halide perovskite solar cells, APL Energy 1 (2023), https://doi.org/10.1063/5.0158216.

[112] P. Luo, X.-Y. Sun, Y. Li, L. Yang, W.-Z. Shao, L. Zhen, C.-Y. Xu, Correlation between structural evolution and device performance of CH3NH3PbI3 solar cells under proton irradiation, ACS Appl. Energy Mater. 4 (2021) 13504–13515, https://doi.org/10.1021/acsaem.1c01958.

[113] A. Bushroa, R. Rahbari, H. Masjuki, M. Muhamad, Approximation of crystallite size and microstrain via XRD line broadening analysis in TiSiN thin films, Vacuum 86 (2012) 1107–1112, https://doi.org/10.1016/j.vacuum.2011.10.011.

[114] T.W. Jones, A. Osherov, M. Alsari, M. Sponseller, B.C. Duck, Y.-K. Jung, C. Settens, F. Niroui, R. Brenes, C.V. Stan, Lattice strain causes non-radiative losses in halide perovskites, Energy Environ. Sci. 12 (2019) 596–606, https://doi.org/10.1039/C8EE02751J.

[115] V. Mote, Y. Purushotham, B. Dole, Williamson-hall analysis in estimation of lattice strain in nanometer-sized ZnO particles, J. Theor. Appl. Phys. 6 (2012) 1–8, https://doi.org/10.1186/2251-7235-6-6.

[116] J.S. Manser, P.V. Kamat, Band filling with free charge carriers in organometal halide perovskites, Nat. Photonics 8 (2014) 737–743, https://doi.org/10.1038/nphoton.2014.171.

[117] M.-J. Choi, Y.-S. Lee, I.H. Cho, S.S. Kim, D.-H. Kim, S.-N. Kwon, S.-I. Na, Functional additives for high-performance inverted planar perovskite solar cells with exceeding 20% efficiency: selective complexation of organic cations in precursors, Nano Energy 71 (2020) 104639, https://doi.org/10.1016/j.nanoen.2020.104639.

[118] H.P. Parkhomenko, M.M. Solovan, S. Sahare, A.I. Mostovyi, D. Aidarkhanov, N. Schopp, T. Kovaliuk, M. Kaikanov, A. Ng, V.V. Brus, Impact of a short-pulse high-intense proton irradiation on high-performance perovskite solar cells, Adv. Funct. Mater. 34 (2024) 2310404, https://doi.org/10.1002/adfm.202310404.

[119] D.W. DeQuilettes, W. Zhang, V.M. Burlakov, D.J. Graham, T. Leijtens, A. Osherov, V. Bulović, H.J. Snaith, D.S. Ginger, S.D. Stranks, Photo-induced halide redistribution in organic–inorganic perovskite films, Nat. Commun. 7 (2016) 11683, https://doi.org/10.1038/ncomms11683.

[120] S. Kanaya, G.M. Kim, M. Ikegami, T. Miyasaka, K. Suzuki, Y. Miyazawa, H. Toyota, K. Osonoe, T. Yamamoto, K. Hirose, Proton irradiation tolerance of high-efficiency perovskite absorbers for space applications, J. Phys. Chem. Lett. 10 (2019) 6990–6995, https://doi.org/10.1021/acs.jpclett.9b02665.

[121] C. Costa, M. Manceau, S. Duzellier, T. Nuns, R. Cariou, Perovskite solar cells under protons irradiation: from in-situ IV-monitoring to root cause degradation elucidation, Sol. Energy Mater. Sol. Cells 257 (2023) 112388, https://doi.org/10.1016/j.solmat.2023.112388.

[122] N.N. Shlenskaya, N.A. Belich, M. Grätzel, E.A. Goodilin, A.B. Tarasov, Light-induced reactivity of gold and hybrid perovskite as a new possible degradation mechanism in perovskite solar cells, J. Mater. Chem. A 6 (2018) 1780–1786, https://doi.org/10.1039/C7TA10217H.

[123] J. Čermák, L. Mihai, D. Sporea, Y. Galagan, J. Fait, A. Artemenko, P. Štenclová, B. Rezek, M. Straticiuc, I. Burducea, Proton irradiation induced changes in glass and polyethylene terephthalate substrates for photovoltaic solar cells, Sol. Energy Mater. Sol. Cells 186 (2018) 284–290, https://doi.org/10.1016/j.solmat.2018.06.046.

[124] M. Saito, F. Nishiyama, K. Kobayashi, S. Nagata, K. Takahiro, Reduction of light elements loss in polymer foils during MeV-proton irradiation by application of an aluminum coating, Nucl. Instrum. Methods Phys. Res., Sect. B 268 (2010) 2918–2922, https://doi.org/10.1016/j.nimb.2010.05.008.

[125] C. Takemasa, T. Chino, R. Ishige, S. Ando, Anisotropic photoconductivity of aromatic and semi-aliphatic polyimide films: effects of charge transfer, molecular orientation, and polymer chain packing, Polymer 180 (2019) 121713, https://doi.org/10.1016/j.polymer.2019.121713.

[126] M. Hasegawa, K. Horie, Photophysics, photochemistry, and optical properties of polyimides, Prog. Polym. Sci. 26 (2001) 259–335, https://doi.org/10.1016/S0079-6700(00)00042-3.

[127] B. Li, W. Zhang, Improving the stability of inverted perovskite solar cells towards commercialization, Commun. Mater. 3 (2022) 65, https://doi.org/10.1038/s43246-022-00291-x.

[128] N. Liu, L. Zhang, Y. Liang, B. Xue, D. Wang, Effects of carrier transport layers on performance degradation in perovskite solar cells under proton irradiation, ACS Appl. Energy Mater. 6 (2023) 6673–6680, https://doi.org/10.1021/acsaem.3c00727.

[129] J.-S. Huang, M.D. Kelzenberg, P. Espinet-González, C. Mann, D. Walker, A. Naqavi, N. Vaidya, E. Warmann, H.A. Atwater, Effects of electron and proton radiation on perovskite solar cells for space solar power application, in: 2017 IEEE 44th Photovoltaic Specialist Conference (PVSC), IEEE, 2017, pp. 1248–1252, https://doi.org/10.1109/PVSC.2017.8366410.

[130] S. Yang, Z. Xu, S. Xue, P. Kandlakunta, L. Cao, J. Huang, Organohalide lead perovskites: more stable than glass under gamma-ray radiation, Adv. Mater. 31 (2019) 1805547, https://doi.org/10.1002/adma.201805547.

[131] H. Huang, W. Qian, C. Dai, Y. Zhao, Y. Liang, R. Lei, X. Wang, S. Yang, J. Xue, Unraveling the degradation and air-induced healing mechanisms of halide perovskites under proton irradiation, ACS Appl. Mater. Interfaces 16 (2024) 65108–65118, https://doi.org/10.1021/acsami.4c16818.

[132] A.M. Oliveira, S. Braccini, P. Casolaro, N. Heracleous, J. Leidner, I. Mateu, F. Murtas, M. Silari, Radiation-induced effects in glass windows for optical readout gem-based detectors, J. Instrum. 16 (2021) T07009, https://doi.org/10.1088/1748-0221/16/07/T07009.

[133] F. Xinjie, S. Lixin, L. Jiacheng, Radiation induced color centers in cerium-doped and cerium-free multicomponent silicate glasses, J. Rare Earths 32 (2014) 1037–1042, https://doi.org/10.1016/S1002-0721(14)60180-0.

[134] B.T. Feleki, R.K. Bouwer, M.M. Wienk, R.A. Janssen, Perovskite solar cells on polymer-coated smooth and rough steel substrates, Sol. RRL 6 (2022) 2100898, https://doi.org/10.1002/solr.202100898.

[135] B.T. Feleki, R.K. Bouwer, V. Zardetto, M.M. Wienk, R.A. Janssen, p–i–n perovskite solar cells on steel substrates, ACS Appl. Energy Mater. 5 (2022) 6709–6715, https://doi.org/10.1021/acsaem.2c00291.

[136] B. Oryema, E. Jurua, I.G. Madiba, I. Ahmad, S.O. Aisida, F.I. Ezema, M. Maaza, Effects of 7 MeV proton irradiation on microstructural, morphological, optical, and electrical properties of fluorine-doped tin oxide thin films, Surf. Interfaces 28 (2022) 101693, https://doi.org/10.1016/j.surfin.2021.101693.

[137] Y.-K. Moon, S. Lee, D.-Y. Moon, W.-S. Kim, B.-W. Kang, J.-W. Park, Effects of proton irradiation on indium zinc oxide-based thin-film transistors, Surf. Coat. Technol. 205 (2010) S109–S114, https://doi.org/10.1016/j.surfcoat.2010.06.030.

[138] K. Ungeheuer, J. Rybak, A.E. Bocirnea, D.A. Pikulski, A.C. Galca, K.W. Marszalek, Influence of proton irradiation on thin films of AZO and ITO transparent conductive oxides—simulation of space environment, Appl. Sci. 15 (2025) 754, https://doi.org/10.3390/app15020754.

[139] S. Svanstrom, T.J. Jacobsson, G. Boschloo, E.M. Johansson, H. Rensmo, U. B. Cappel, Degradation mechanism of silver metal deposited on lead halide perovskites, ACS Appl. Mater. Interfaces 12 (2020) 7212–7221, https://doi.org/10.1021/acsami.9b20315.

[140] P. Giri, J. Tiwari, Silicon-perovskite combinational solar cells degradation phenomena for futuristic IOTs powering, Discov. Appl. Sci. 7 (2025) 1–13, https://doi.org/10.1007/s42452-025-06476-6.

[141] D. Hughes, S.M. Meroni, J. Barbé, D. Raptis, H.K. Lee, K.C. Heasman, F. Lang, T. M. Watson, W.C. Tsoi, Proton radiation hardness of perovskite solar cells utilizing a mesoporous carbon electrode, Energy Technol. 9 (2021) 2100928, https://doi.org/10.1002/ente.202100928.

[142] L.E. Mundt, J. Tong, A.F. Palmstrom, S.P. Dunfield, K. Zhu, J.J. Berry, L. T. Schelhas, E.L. Ratcliff, Surface-activated corrosion in tin–lead halide perovskite solar cells, ACS Energy Lett. 5 (2020) 3344–3351, https://doi.org/10.1021/acsenergylett.0c01445.

[143] R. Prasanna, T. Leijtens, S.P. Dunfield, J.A. Raiford, E.J. Wolf, S.A. Swifter, J. Werner, G.E. Eperon, C. de Paula, A.F. Palmstrom, Design of low bandgap tin–lead halide perovskite solar cells to achieve thermal, atmospheric and operational stability, Nat. Energy 4 (2019) 939–947, https://doi.org/10.1038/s41560-019-0471-6.

[144] T. Markvart, Radiation damage in solar cells, J. Mater. Sci. Mater. Electron. 1 (1990) 1–12, https://doi.org/10.1007/BF00716008.

[145] A.K. Jena, Y. Numata, M. Ikegami, T. Miyasaka, Role of spiro-OMeTAD in performance deterioration of perovskite solar cells at high temperature and reuse of the perovskite films to avoid Pb-waste, J. Mater. Chem. A 6 (2018) 2219–2230, https://doi.org/10.1039/C7TA07674F.

[146] R.S. Sanchez, E. Mas-Marza, Light-induced effects on Spiro-OMeTAD films and hybrid lead halide perovskite solar cells, Sol. Energy Mater. Sol. Cells 158 (2016) 189–194, https://doi.org/10.1016/j.solmat.2016.03.024.

[147] V. Golovanov, L. Khirunenko, A. Kiv, D. Fuks, M. Soshin, G. Korotchenkov, Radiation effects in SnO2–Si sensor structures, Radiat. Eff. Defect Solid 161 (2006) 85–89, https://doi.org/10.1080/10420150500493501.

[148] Q. Jiang, X. Zhang, J. You, SnO2: a wonderful electron transport layer for perovskite solar cells, Small 14 (2018) 1801154, https://doi.org/10.1002/smll.201801154.

[149] L. Shi, M.P. Bucknall, T.L. Young, M. Zhang, L. Hu, J. Bing, D.S. Lee, J. Kim, T. Wu, N. Takamure, Gas chromatography–mass spectrometry analyses of encapsulated stable perovskite solar cells, Science 368 (2020) eaba2412, https://doi.org/10.1126/science.aba2412.

[150] M.-D. Zhang, D.-X. Zhao, L. Chen, N. Pan, C.-Y. Huang, H. Cao, M.-D. Chen, Structure-performance relationship on the asymmetric methoxy substituents of spiro-OMeTAD for perovskite solar cells, Sol. Energy Mater. Sol. Cells 176 (2018) 318–323, https://doi.org/10.1016/j.solmat.2017.10.014.

[151] Z. Hawash, L.K. Ono, Y. Qi, Recent advances in spiro-MeOTAD hole transport material and its applications in organic–inorganic halide perovskite solar cells, Adv. Mater. Interfac. 5 (2018) 1700623, https://doi.org/10.1002/admi.201700623.

[152] B. Xue, L. Zhang, T. Zhang, N. Liu, A. Ejaz, Y. Liang, Degradation behavior and damage mechanisms of perovskite solar cells under 50–200 keV proton irradiations, Sol. Energy Mater. Sol. Cells 282 (2025) 113442, https://doi.org/10.1016/j.solmat.2025.113442.

[153] R.A. Kerner, A.V. Cohen, Z. Xu, A.R. Kirmani, S.Y. Park, S.P. Harvey, J.P. Murphy, R.C. Cawthorn, N.C. Giebink, J.M. Luther, Electrochemical doping of halide perovskites by noble metal interstitial cations, Adv. Mater. 35 (2023) 2302206, https://doi.org/10.1002/adma.202302206.

[154] A.R. Kirmani, T.A. Byers, Z. Ni, K. VanSant, D.K. Saini, R. Scheidt, X. Zheng, T. B. Kum, I.R. Sellers, L. McMillon-Brown, Unraveling radiation damage and healing mechanisms in halide perovskites using energy-tuned dual irradiation dosing, Nat. Commun. 15 (2024) 696, https://doi.org/10.1038/s41467-024-44876-1.

[155] Z. Li, C. Xiao, Y. Yang, S.P. Harvey, D.H. Kim, J.A. Christians, M. Yang, P. Schulz, S.U. Nanayakkara, C.-S. Jiang, Extrinsic ion migration in perovskite solar cells, Energy Environ. Sci. 10 (2017) 1234–1242, https://doi.org/10.1039/C7EE00358G.

[156] G. Parthasarathy, C. Shen, A. Kahn, S. Forrest, Lithium doping of semiconducting organic charge transport materials, J. Appl. Phys. 89 (2001) 4986–4992, https://doi.org/10.1063/1.1359161.

[157] I.V. Martynov, A.V. Akkuratov, S.Y. Luchkin, S.A. Tsarev, S.D. Babenko, V. G. Petrov, K.J. Stevenson, P.A. Troshin, Impressive radiation stability of organic solar cells based on fullerene derivatives and carbazole-containing conjugated polymers, ACS Appl. Mater. Interfaces 11 (2019) 21741–21748, https://doi.org/10.1021/acsami.9b01729.

[158] W. Hui, X. Kang, B. Wang, D. Li, Z. Su, Y. Bao, L. Gu, B. Zhang, X. Gao, L. Song, Stable electron-transport-layer-free perovskite solar cells with over 22% power conversion efficiency, Nano Lett. 23 (2023) 2195–2202, https://doi.org/10.1021/acs.nanolett.2c04720.

[159] Z. Yu, B. Chen, P. Liu, C. Wang, C. Bu, N. Cheng, S. Bai, Y. Yan, X. Zhao, Stable organic–inorganic perovskite solar cells without hole-conductor layer achieved via cell structure design and contact engineering, Adv. Funct. Mater. 26 (2016) 4866–4873, https://doi.org/10.1002/adfm.201504564.

[160] D. Li, C. Liu, S. Chen, W. Kong, H. Zhang, D. Wang, Y. Li, J. Chang, C. Cheng, Simplified compact perovskite solar cells with efficiency of 19.6% via interface engineering, Energy Environ. Mater. 3 (2020) 5–11, https://doi.org/10.1002/eem2.12063.

[161] W. Kong, W. Li, C. Liu, H. Liu, J. Miao, W. Wang, S. Chen, M. Hu, D. Li, A. Amini, Organic monomolecular layers enable energy-level matching for efficient hole transporting layer free inverted perovskite solar cells, ACS Nano 13 (2019) 1625–1634, https://doi.org/10.1021/acsnano.8b07627.

[162] Y. Huang, T. Liu, C. Liang, J. Xia, D. Li, H. Zhang, A. Amini, G. Xing, C. Cheng, Towards simplifying the device structure of high-performance perovskite solar cells, Adv. Funct. Mater. 30 (2020) 2000863, https://doi.org/10.1002/adfm.202000863.

[163] S.F. Völker, S. Collavini, J.L. Delgado, Organic charge carriers for perovskite solar cells, ChemSusChem 8 (2015) 3012–3028, https://doi.org/10.1002/cssc.201500742.

[164] H. Wei, D. DeSantis, W. Wei, Y. Deng, D. Guo, T.J. Savenije, L. Cao, J. Huang, Dopant compensation in alloyed CH3NH3PbBr3− x Cl x perovskite single crystals for gamma-ray spectroscopy, Nat. Mater. 16 (2017) 826–833, https://doi.org/10.1038/nmat4927.

[165] W.-J. Yin, T. Shi, Y. Yan, Unusual defect physics in CH3NH3PbI3 perovskite solar cell absorber, Appl. Phys. Lett. 104 (2014), https://doi.org/10.1063/1.4864778.

[166] Q. Wang, Y. Shao, H. Xie, L. Lyu, X. Liu, Y. Gao, J. Huang, Qualifying composition dependent p and n self-doping in CH3NH3PbI3, Appl. Phys. Lett. 105 (2014), https://doi.org/10.1063/1.4899051.

[167] J. Vollbrecht, J. Lee, S.-J. Ko, V.V. Brus, A. Karki, W. Le, M. Seifrid, M.J. Ford, K. Cho, G.C. Bazan, Design of narrow bandgap non-fullerene acceptors for photovoltaic applications and investigation of non-geminate recombination dynamics, J. Mater. Chem. C 8 (2020) 15175–15182, https://doi.org/10.1039/D0TC02136A.

[168] D. Glowienka, Y. Galagan, Light intensity analysis of photovoltaic parameters for perovskite solar cells, Adv. Mater. 34 (2022) 2105920, https://doi.org/10.1002/adma.202105920.

[169] V. Brus, Light dependent open-circuit voltage of organic bulk heterojunction solar cells in the presence of surface recombination, Org. Electron. 29 (2016) 1–6, https://doi.org/10.1016/j.orgel.2015.11.025.

[170] J. Vollbrecht, V.V. Brus, On the recombination order of surface recombination under open circuit conditions, Org. Electron. 86 (2020) 105905, https://doi.org/10.1016/j.orgel.2020.105905.

[171] J. Vollbrecht, V.V. Brus, Effects of recombination order on open-circuit voltage decay measurements of organic and perovskite solar cells, Energies 14 (2021) 4800, https://doi.org/10.3390/en14164800.

[172] C.M. Proctor, M. Kuik, T.-Q. Nguyen, Charge carrier recombination in organic solar cells, Prog. Polym. Sci. 38 (2013) 1941–1960, https://doi.org/10.1016/j.progpolymsci.2013.08.008.

[173] W.J. Potscavage Jr., A. Sharma, B. Kippelen, Critical interfaces in organic solar cells and their influence on the open-circuit voltage, Acc. Chem. Res. 42 (2009) 1758–1767, https://doi.org/10.1021/ar900139v.

[174] X. Zhou, H. Wu, B. Lin, H.B. Naveed, J. Xin, Z. Bi, K. Zhou, Y. Ma, Z. Tang, C. Zhao, Different morphology dependence for efficient indoor organic photovoltaics: the role of the leakage current and recombination losses, ACS Appl. Mater. Interfaces 13 (2021) 44604–44614, https://doi.org/10.1021/acsami.1c09600.

[175] K. Tvingstedt, L. Gil-Escrig, C. Momblona, P. Rieder, D. Kiermasch, M. Sessolo, A. Baumann, H.J. Bolink, V. Dyakonov, Removing leakage and surface recombination in planar perovskite solar cells, ACS Energy Lett. 2 (2017) 424–430, https://doi.org/10.1021/acsenergylett.6b00719.

[176] C.M. Proctor, T.-Q. Nguyen, Effect of leakage current and shunt resistance on the light intensity dependence of organic solar cells, Appl. Phys. Lett. 106 (2015), https://doi.org/10.1063/1.4913589.

[177] H.P. Parkhomenko, A.I. Mostovyi, G. Akhtanova, M.M. Solovan, M. Kaikanov, N. Schopp, V.V. Brus, Self-healing of proton-irradiated organic photodiodes and photovoltaics, Adv. Energy Mater. 13 (2023) 2301696, https://doi.org/10.1002/aenm.202301696.

[178] V.V. Brus, C.M. Proctor, N.A. Ran, T.Q. Nguyen, Capacitance spectroscopy for quantifying recombination losses in nonfullerene small-molecule bulk heterojunction solar cells, Adv. Energy Mater. 6 (2016) 1502250, https://doi.org/10.1002/aenm.201502250.

[179] V.V. Brus, N. Schopp, S.J. Ko, J. Vollbrecht, J. Lee, A. Karki, G.C. Bazan, T. Q. Nguyen, Temperature and light modulated open-circuit voltage in nonfullerene organic solar cells with different effective bandgaps, Adv. Energy Mater. 11 (2021) 2003091, https://doi.org/10.1002/aenm.202003091.

[180] W.-Q. Wu, Z. Yang, P.N. Rudd, Y. Shao, X. Dai, H. Wei, J. Zhao, Y. Fang, Q. Wang, Y. Liu, Bilateral alkylamine for suppressing charge recombination and improving stability in blade-coated perovskite solar cells, Sci. Adv. 5 (2019) eaav8925, https://doi.org/10.1126/sciadv.aav8925.

[181] S.M. Sze, Y. Li, K.K. Ng, Physics of Semiconductor Devices, John wiley & sons, 2021.

[182] W. Liu, J. Zheng, M. Shang, Z. Fang, K.-C. Chou, W. Yang, X. Hou, T. Wu, Electron-beam irradiation-hard metal-halide perovskite nanocrystals, J. Mater. Chem. A 7 (2019) 10912–10917, https://doi.org/10.1039/C9TA01898K.

[183] J. Haruyama, K. Sodeyama, L. Han, Y. Tateyama, First-principles study of ion diffusion in perovskite solar cell sensitizers, J. Am. Chem. Soc. 137 (2015) 10048–10051, https://doi.org/10.1021/jacs.5b03615.

[184] J. Xing, Q. Wang, Q. Dong, Y. Yuan, Y. Fang, J. Huang, Ultrafast ion migration in hybrid perovskite polycrystalline thin films under light and suppression in single crystals, Phys. Chem. Chem. Phys. 18 (2016) 30484–30490, https://doi.org/10.1039/C6CP06496E.

[185] N.H. Nickel, F. Lang, V. Brus, J. Bundesmann, S. Seidel, A. Denker, S. Albrecht, G. Landi, H. Neitzert, Radiation hardness and self-healing of perovskite solar cells under proton irradiation (conference presentation), in: Physics, Simulation, and Photonic Engineering of Photovoltaic Devices, VII, SPIE, 2018 1052703, https://doi.org/10.1117/12.2290241.

[186] D.R. Ceratti, Y. Rakita, L. Cremonesi, R. Tenne, V. Kalchenko, M. Elbaum, D. Oron, M.A.C. Potenza, G. Hodes, D. Cahen, Self-healing inside APbBr3 halide perovskite crystals, Adv. Mater. 30 (2018) 1706273, https://doi.org/10.1002/adma.201706273.

[187] D.-Y. Son, J.-W. Lee, Y.J. Choi, I.-H. Jang, S. Lee, P.J. Yoo, H. Shin, N. Ahn, M. Choi, D. Kim, Self-formed grain boundary healing layer for highly efficient CH3NH3PbI3 perovskite solar cells, Nat. Energy 1 (2016) 1–8, https://doi.org/10.1038/nenergy.2016.81.

[188] P. Li, H. Dong, J. Lan, Y. Bai, C. He, L. Ma, Y. Li, J. Liu, Tolerance of perovskite solar cells under proton and electron irradiation, Materials 15 (2022) 1393, https://doi.org/10.3390/ma15041393.

[189] M.N. Khanal, V.R. Whiteside, H. Afshari, M. Parashar, M. Sharma, G.E. Eperon, Y. Kuang, S. Hamtaei, B. Vermang, B. Rout, Perovskite solar cells for space: assessment of encapsulation under proton irradiation, in: 2024 IEEE 52nd Photovoltaic Specialist Conference (PVSC), IEEE, 2024, pp. 403–406, https://doi.org/10.1109/PVSC57443.2024.10749616.

[190] M. Jamal, S. Shahahmadi, M.A.A. Wadi, P. Chelvanathan, N. Asim, H. Misran, M. Hossain, N. Amin, K. Sopian, M. Akhtaruzzaman, Effect of defect density and energy level mismatch on the performance of perovskite solar cells by numerical simulation, Optik 182 (2019) 1204–1210, https://doi.org/10.1016/j.ijleo.2018.12.163.

[191] S. Rai, B. Pandey, D. Dwivedi, Modeling of highly efficient and low cost CH3NH3Pb (I1-xClx) 3 based perovskite solar cell by numerical simulation, Opt. Mater. 100 (2020) 109631, https://doi.org/10.1016/j.optmat.2019.109631.

[192] T. Ouslimane, L. Et-Taya, L. Elmaimouni, A. Benami, Impact of absorber layer thickness, defect density, and operating temperature on the performance of MAPbI3 solar cells based on ZnO electron transporting material, Heliyon 7 (2021) e06379, https://doi.org/10.1016/j.heliyon.2021.e06379.